Ares J. Rosakis[1]
Graduate Aerospace Laboratories,
California Institute of Technology,
Pasadena, CA 91125
e-mail: arosakis@caltech.edu

José E. Andrade
Mechanical and Civil Engineering,
California Institute of Technology,
Pasadena, CA 91125
e-mail: jandrade@caltech.edu

Vahe Gabuchian
Graduate Aerospace Laboratories,
California Institute of Technology,
Pasadena, CA 91125
e-mail: gabuchian@caltech.edu

John M. Harmon
Mechanical and Civil Engineering,
California Institute of Technology,
Pasadena, CA 91125
e-mail: jhharmon@caltech.edu

Joel P. Conte
Department of Structural Engineering,
University of California,
San Diego, CA 92093
e-mail: jpconte@ucsd.edu

José I. Restrepo
Department of Structural Engineering,
University of California,
San Diego, CA 92093
e-mail: jrestrepo@ucsd.edu

Andrés Rodriguez
Department of Structural Engineering,
University of California,
San Diego, CA 92093
e-mail: a1rodrig@ucsd.edu

Arpit Nema
Pacific Earthquake Engineering Research Center,
University of California,
Berkeley, CA 94804
e-mail: anema@berkeley.edu

Andrea R. Pedretti
Energy Vault, Inc.,
Westlake Village, CA 91361
e-mail: andrea@energyvault.com

Implications of Buckingham's Pi Theorem to the Study of Similitude in Discrete Structures: Introduction of the R_F^N, μ^N, and S^N Dimensionless Numbers and the Concept of Structural Speed

Motivated by the need to evaluate the seismic response of large-capacity gravity energy storage systems (potential energy batteries) such as the proposed frictional Multiblock Tower Structures (MTS) recently discussed by Andrade et al. (2021, "Seismic Performance Assessment of Multiblock Tower Structures As Gravity Energy Storage Systems," ASME J. Appl. Mech., Submitted), we apply Buckingham's Pi theorem (Buckingham, E., 1914, "On Physically Similar Systems; Illustrations of the Use of Dimensional Equations," Phys. Rev., 4, pp. 345–376) to identify the most general forms of dimensionless numbers and dynamic similitude laws appropriate for scaling discontinuous multiblock structural systems involving general restoring forces resisting inertial loading. We begin by introducing the dimensionless "mu-number" (μ^N) appropriate for both gravitational and frictional restoring forces and then generalize by introducing the "arbitrary restoring force number" (R_F^N). R_F^N is subsequently employed to study similitude in various types of discontinuous or discrete systems featuring frictional, gravitational, cohesive, elastic, and mixed restoring forces acting at the block interfaces. In the process, we explore the additional consequences of inter and intra-block elasticity on scaling. We also formulate a model describing the mechanism of structural signal transmission for the case of rigid MTS featuring inter-block restoring forces composed of elastic springs and interfacial friction, introducing the concept of "structural speed." Finally, we validate our results by demonstrating that dynamic time-histories of field quantities and structural speeds between MTS models at various scales are governed by our proposed similitude laws, thus demonstrating the consistency of our approach. [DOI: 10.1115/1.4051338]

Keywords: discontinuous system, discrete frictional structures, dynamic similitude, scaling, seismic testing

1 Introduction

In this paper, we introduce and experimentally validate the most general theoretical framework governing the dynamic behavior and scaling of multiblock tower structures (MTS) as dictated by the application of Buckingham's Pi theorem (BPT) [1]. BPT is a mathematically formal tool used in all branches of engineering and science to identify dimensionless groups of problem variables crucial in determining the response of a physical system when it is subjected to excitations in a particular environment. The ability of identifying dimensionless groups is particularly important for studying very complex systems where closed-form relations describing their behaviors are not available. These groups allow for the prediction of dominant trends between crucial parameters. In addition, the identification of the dimensionless groups, or dimensionless numbers, enables the design of "scaled" or "model" experiments, which can be used to indirectly, but accurately, study "prototype" system behavior by just observing the

[1]Corresponding author.

Contributed by the Applied Mechanics Division of ASME for publication in the Journal of Applied Mechanics. Manuscript received May 5, 2021; final manuscript received May 13, 2021; published online July 12, 2021. Assoc. Editor: Yonggang Huang.

behavior of a model. This becomes possible, since knowledge of the appropriate dimensionless groups dictates the form of "similitude" or scaling laws and thus allows observations obtained at a small scale, in a controlled and highly instrumented environment, to be extrapolated to the often much larger engineering or geophysical scale without loss of accuracy.

Historically, the above approach was extensively used in fluid dynamics and in thermal sciences [2–4] where scaling enabled the use of wind-tunnel and water-tunnel testing driving the design of generations of aircraft and submarine systems at a time when large scale numerical computations were unavailable. A prominent example of dimensionless numbers used in scaling of fluid mechanics and gas dynamics systems is the Reynold's number ($R_e^N := v\ell/\nu$) which represents the ratio of fluid inertia to the viscous restoring forces and characterizes the complex transition between laminar and turbulent flow. Other examples are the Mach number ($M^N := v/c$), which is a measure of the compressibility characteristics of fluid flow past an object moving at a certain speed, and the Froude number ($F_r^N := v/\sqrt{\ell g}$), which represents the ratio of inertial to gravitational restoring forces. In the above examples, v represents a measure of fluid speed, c is the local speed of sound, ν is the kinematic viscosity, ℓ is a characteristic length while g, only involved in F_r^N, is the acceleration of gravity. In fluids, F_r^N scaling is primarily used in analyzing hydraulic systems characterizing the nature of free-surface flows or gravity wave formation in tsunamigenesis. It has also been used to scale the wave making resistance of similar floating bodies of various sizes. In contrast to fluid dynamics and thermal sciences, the fields of solid mechanics and structures have only made limited use of dimensionless numbers and scaling, with notable exceptions such as the introduction of scaling laws governing ductility, instabilities, and fractures [5,6]. Other prominent exceptions to this rule can be found in structural dynamics and in earthquake seismology, where the use of just a few key dimensionless numbers has enabled the effective testing of the resistance of buildings to earthquake excitation through scaled-down shake table experiments (extensively discussed by Harris and Sabnis [7]). For such testing, the most commonly used dimensionless number is the Cauchy number ($C^N := v/\sqrt{E/\rho} = v/c$), where v is a measure of the particle velocity of a solid or structure, ρ is the mass density, and E and c are representative moduli and elastic wave speeds of the material. The C^N number represents the ratio of the inertial forces acting on various parts of the system to the elastic restoring forces provided by the system's elasticity. In very limited cases, the Froude number (mostly in combination with C^N scaling) has also been used to scale model/prototype systems and to test structures when gravitational restoring forces are also considered important (see Moncarz and Krawinkler [8]).

To understand the reasons for the widespread use of C^N scaling in evaluating the seismic reliability of the built environment in modern times and to also explain the motivation of the current study, we now refer to Fig. 1. This figure pictorially describes the major types of large "monumental" structures that humanity has constructed in the last 46 or so centuries [9–12], most of which have experienced and need to be protected from seismic excitation of various types and intensities. Figures 1(*a*) and 1(*b*) depict early monumental structures made of various quarried geomaterials such as limestone, sandstone, granite, syenite, alabaster, and basalt as is the case with the Egyptian pyramids, or limestone, sandstone, or marble as is the case of ancient Greek or Roman temples. With time, and up to the past century, more monumental structures were built out of various combinations of rocks and raw and baked

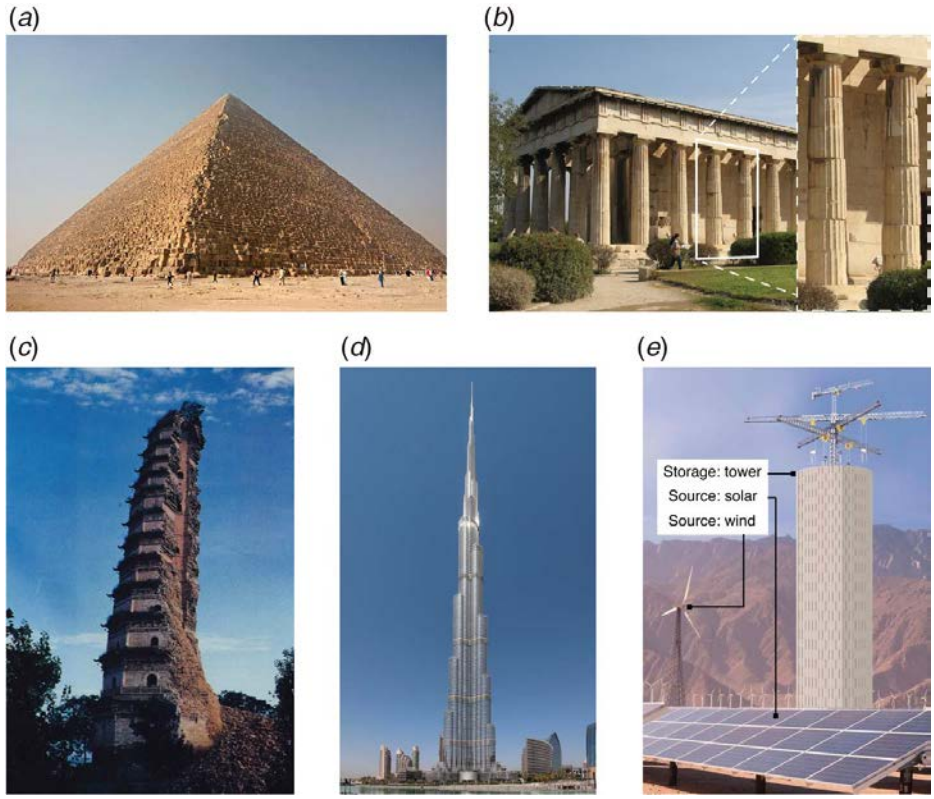

Fig. 1 Pictorial description of the evolution of the major types of large structures throughout the centuries. Progression from (*a*)–(*c*) discontinuous, frictional/gravitational rigid multiblock systems to (*d*) continuous, flexible structures and, recently, back to (*e*) discontinuous, frictional/gravitational energy storage systems. From left to right, (*a*) the Great Pyramid of Giza in Cairo, Egypt, circa 2500 BC, (*b*) the Temple of Hephaistos in Athens, Greece, circa 415 BC, (*c*) the Famen Pagoda in Shaanxi, China, circa 200 AD, (*d*) the Burj Khalifa in Dubai, United Arab Emirates, 2010 AD, and (*e*) the proposed gravitational energy storage system motivating this study.

mud bricks as is the case in the damaged pagoda depicted in Fig. 1(*c*). In all cases shown in Figs. 1(*a*)–1(*c*), the structures were characterized by the high density and rigidity of the constituent materials. These structures belong to the class of "discontinuous" or "discrete" gravitational structures in which a variety of nearly rigid elements are held together by either frictional or cohesive (mortar) restoring forces. These forces act at multiple interfaces and, in addition to gravity, provide the restoring forces and moments during seismic excitation. It is the competition between the seismically induced inertial forces with the various restoring forces (gravitational, frictional, cohesive) described above as well as the ability of the interfaces to dissipate energy, which ultimately determines the ability of these discontinuous structures to resist earthquake damage.

This competition, along with the associated kinematic response of rocking, sliding, and its combinations, has been studied in relation to either monolithic or segmented column systems by a number of authors (e.g., Refs. [13–23]), providing valuable insight regarding their dynamic response. Most notably, the behavior of single multi-spondyle marble columns has been shown to perform very well under seismic excitation compared to the monolithic equivalent as shown in a recent numerical study by Konstantinidis et al. [23] and analytical studies by Kounadis et al. [21,22] and the references therein. With this observation in mind, it is perhaps not surprising that a large number of ancient gravitational/frictional structures all around the Mediterranean, such as the Temple of Athena (Korres [24]) and the Hephaistion Temple in Athens (Stiros [25]), depicted here in Fig. 1(*b*), have sustained damage but have ultimately survived over 25 centuries of intense tectonic activity. Their survival is due to the ability of their many interfaces to provide multiple distributed sites of energy dissipation. Clear evidence of frictional sliding of marble column drums sustained by the still intact Hephaistion temple is visible in the inset of Fig. 1(*b*) and discussed by Stiros [25] and Galanopoulos [26]. Moving on to the modern era, the ability to manufacture lighter, flexible but also high-strength materials at low-cost, combined with the need of cheaper construction, has allowed the use of reinforced concrete and steel frame structures enabling construction of high-rise buildings of great height and seismic resilience of the type shown in Fig. 1(*d*). These new, continuous structures, unlike their discrete, frictional or cohesive counterparts of the past, depend on their elastic flexibility and ultimately on their strength to resist seismic loading by initially providing elastic restoring forces. The continuity and the elastic flexibility of these systems makes the Cauchy number C^N the appropriate dimensionless quantity governing their seismic behavior. Indeed, continuous structures have dominated the built environment since the beginning of the 20th century and will likely continue constituting the norm until new needs and applications emerge.

One such very recent application arises from the urgent need to provide large-capacity energy storage systems. Such systems can be employed near a green energy source, such as solar and wind, both of which suffer from intermittent energy generation. These systems need to be simple, resilient, and easily deployable all around the world. Figure 1(*e*) shows the concept of one such system recently proposed by Energy Vault, Inc. [27]. In this system, thousands of massive blocks of a soil/concrete/disposable waste mix are lifted by cranes during periods of high energy availability (e.g., peak wind or sunlight), visible in the illustration, and are stacked on top of each other to construct a high tower (up to 160 m) by using the excess of the generated green energy. This results in the conversion of harvested energy into potential energy stored in the MTS [28]. During periods of low energy harvesting or peak user need, the same cranes are used to deconstruct the MTS in a controlled manner, converting the stored potential energy into kinetic energy used to generate electricity, thus making it available to the grid at times of high demand. The conversion efficiency of the energy storage/delivery cycle is just above 80%. These simple towers are discontinuous and purely frictionally held, therefore very similar to the ancient discontinuous structures described in Figs. 1(*a*)–1(*c*). Very much like their ancient counterparts, these new systems feature nearly rigid blocks and thousands of dissipative interfaces. When subjected to seismic excitation, the resulting inertial forces on each block are resisted by both gravitational forces and moments as well as frictional restoring forces with limited elastic resistance offered either by the interfaces or by the nearly rigid blocks. Interestingly, after almost 46 centuries of evolution in construction methods, this newly emerging energy storage method (the gravitational battery) brings us back full-circle to the re-emergence of fully discontinuous frictional systems. Success highlights the need of properly understanding their seismic performance, thus necessitating the identification of dimensionless numbers that govern their dynamic behavior. Unlike the flexible continuous systems of Fig. 1(*c*), the Cauchy number and scaling based on the assumption of system continuity and elasticity is totally inappropriate in describing the dynamics of such grossly discontinuous and dissipative structures. Furthermore, as we will show in this paper, Froude number (F_r^N) type of scaling, although very appropriate for scaling purely gravitational block systems as shown in Ref. [19], does not incorporate the correct physics of energy dissipation when frictional sliding is present and is, thus, of only limited applicability to frictional systems. To our knowledge, no general analysis has previously been proposed to rigorously scale the dynamics of discontinuous structures such as MTS. Indeed, this new energy storage application has motivated our work. Our goal is to identify the wider family of dimensionless numbers describing the dynamics of all types of rigid or elastic discontinuous structures, ancient or new, involving various restoring forces, including the important case of frictional restoring forces. In addition, the present study provides the theoretical framework which informs the consistency of the multiscale experimental design [29,30] and modeling strategies [31] employed in a recent campaign aimed at evaluating the seismic response of discrete, frictional MTS [28]. Here, we define consistency as the ability to compare physical and virtual models across scales and material properties.

1.1 Approximate Statement of Buckingham's Pi Theorem.

Assume that $q_1, q_2, q_3, \ldots, q_m$ are m dimensional variables describing the behavior of a physical problem, or system, through the equation $f(q_1; \ldots; q_m) = 0$. Further, if n is the number of fundamental dimensions (e.g., charge [Q], mass [M], length [L], time [T]) required to describe all of the m variables, then one can arbitrarily choose n number of variables out of the original m variables of the system and call them "primary" or "repeated" variables. The "remaining" $(m-n)$ variables can then be expressed as non-dimensional combinations of the n "primary" variables. These combinations are called the Π groups $(\Pi_1, \Pi_2, \ldots, \Pi_{m-n})$ and are $(m-n)$ in number, each involving one of the "remaining" variables. Furthermore, the original physical problem can be expressed as

$$F(\Pi_1; \Pi_2; \ldots; \Pi_{m-n}) = 0$$

and each of the Π groups can be expressed as a function of the rest, i.e., $\Pi_1 = \Pi_1\,(\Pi_2; \Pi_3; \ldots; \Pi_{m-n})$, $\Pi_2 = \Pi_2(\Pi_1; \Pi_3; \ldots; \Pi_{m-n})$, etc.

1.2 Applying Buckingham's Pi Theorem to Various Discrete Systems.

Consider a discrete MTS system or structure of characteristic length (say total height) ℓ, composed of various contacting pieces, or blocks whose height ℓ_0, as well as other dimensions scale with ℓ and have a mass density ρ. The pieces are initially at rest in the presence of a gravitational field of gravitational acceleration "g." A laboratory model of such a system is shown in Fig. 2(*a*).

We will examine the implications of BPT when such a discrete structure is subjected to a specific inertial excitation in the presence of a gravitational field. During dynamic loading, and if the acceleration is denoted by a, the resulting "inertial" force per unit volume, or body force density ρa of each of the contacting pieces is resisted by

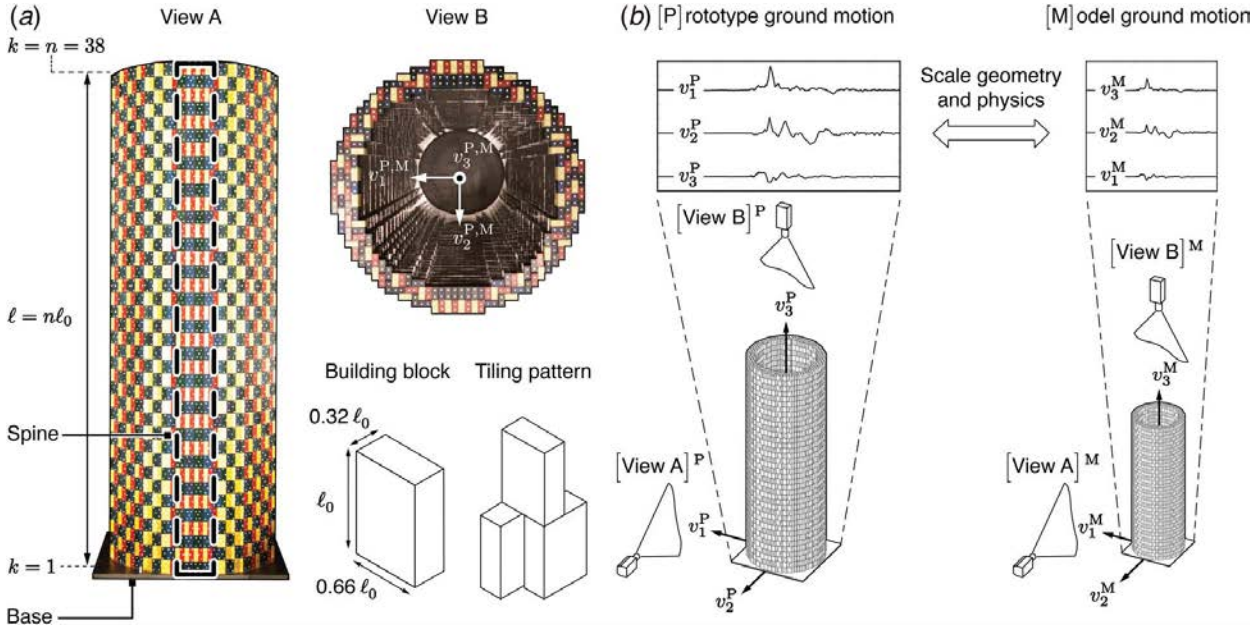

Fig. 2 An aluminum (Al) laboratory model (*a*) of a Multiblock Tower Structure (MTS) [28], or potential energy battery, used in large-capacity energy storage. Both model and prototype systems are composed of 7144 blocks. The prototype tower may reach 160 m in height. The towers comprise 38 stories (188 blocks each) and are constructed during periods of peak energy harvesting by following a repeated tiling pattern of the type shown. The potential energy stored is recovered during periods of peak energy demand by deconstructing the tower. (*b*) Exploring the seismic response of such a discontinuous structure by using geometrically similar, scaled-down models in the laboratory necessitates the appropriate scaling of the ground velocity (or acceleration) time-histories both in amplitude and time as shown in (*b*). The identification of dimensionless numbers describing the physics of this dynamic problem informs the scaling and results in model/prototype similitude. The optical diagnostics are also scaled.

(1) a restoring "gravitational" force density $f_r = \rho g$ at the interface of rigid blocks (Case 1),
(2) a restoring, Coulomb-like "frictional" force density $f_r = \mu_s \rho g$ at the interface of rigid blocks (Case 2),
(3) an "arbitrary" restoring force density f_r at the interface of rigid blocks (Case 3), or
(4) an arbitrary restoring force density f_r at the interface of "elastic" blocks (Case 4).

In Cases 1 and 2, the "restoring" force density per unit volume can generally be expressed as $\mu\rho g$, where $\mu = 1$ for Case 1 and $\mu = \mu_s$ (coefficient of friction) for Case 2.

We first consider Cases 1 and 2 above by further assuming that the system is purely rigid (infinite block and block-interface stiffness or equivalently, infinite wave speeds). We then extend the analysis to a third case (Case 3) in which the rigid blocks interact with each other through arbitrary restoring forces f_r, including cohesive, frictional or gravitational interfacial restoring forces. Finally, the most general case of discrete blocks will be considered (Case 4) in which the discrete structure is also allowed to deform elastically (through bulk elasticity or equivalent springs) while their interfacial restoring forces will be kept arbitrary, e.g., elastic, cohesive, frictional, and gravitational. The implication of each of these cases will be discussed and new non-dimensional numbers R_F^N, μ^N, and S^N will be introduced. We also examine the consequence of all of these cases to similitude requirements between "prototype" and "model" systems of the type shown in Fig. 2(*a*). We then validate our approach by comparing time histories of kinematic fields of similar model/prototype systems subjected to scaled earthquake excitations as shown in Fig. 2(*b*).

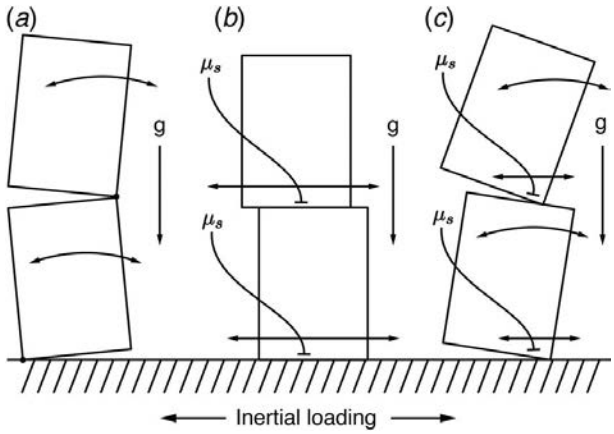

Fig. 3 Basic kinematics of (*a*) rocking, (*b*) frictional sliding, and (*c*) frictional rock/sliding of individual blocks within a multiblock structure

2 Applying Buckingham's Pi Theorem to Discrete Systems of Gravitationally and Frictionally Held Rigid Blocks (Cases 1 and 2)

Figure 2 depicts a particular geometry of a (*a*) discrete MTS which is subjected to (*b*) ground velocity histories $v_i(t)$ at its base. Depending on the nature of the ground excitation at the tower base as well as the inter-block frictional characteristics, each block will rock, slide, and rock/slide (with or without friction) as schematically depicted in Fig. 3. In Case 1, the rigid blocks are allowed to rock and contact with no frictional dissipation allowed. The acceleration field of the structure results in "inertial" force densities ρa. These inertial forces and associated moment densities are resisted by "gravitational" restoring force ρg and moment $\rho g \ell$ densities.

In this case, the most general dynamic problem involves the variables a, t, ℓ, g, and ρ as dictated by Newton's laws and kinematics,

but can also alternatively be described by the following equivalent set of five variables:

$$v;\ a;\ \ell;\ g;\ \rho\ (m=5) \tag{1}$$

where v and a are particle velocities and accelerations, respectively, t is the time, ℓ is a characteristic length, and ρ is the material mass density.

In Case 2, rigid blocks are allowed to slide and rock/slide with friction. The acceleration field of the structure results in "inertial" force densities ρa. These "inertial" forces are resisted by "frictional" restoring force densities $\rho(\mu_s g)$. This is very similar to Case 1, the only difference being that the physics of sliding also involve an additional interfacial property in the form of the frictional coefficient μ_s, which is in general different than unity.

Here, the most general problem would involve the following six variables:

$$v;\ a;\ \ell;\ \mu_s;\ g;\ \rho\ (m=6) \tag{2}$$

However, since μ_s is dimensionless, it cannot be stated as one of the dimensional variables needed to implement BPT.

In an attempt to introduce some knowledge from physics into our consideration, we first contrast the two "restoring" force densities (ρg) and $(\rho\mu_s g)$ for Cases 1 and 2, respectively, and observe that because of the nature of Coulomb-like frictional resistance, which is proportional to normal load, both force densities are proportional to (ρg). In Case 1, the coefficient of proportionality is unity, whereas in Case 2, it is equal to μ_s. This observation allows us to couple the non-dimensional number μ_s with g as $(\mu_s g)$ and thus to list the following dimensional variables for problems of the type relevant to Case 2:

$$v;\ a;\ \ell;\ (\mu_s g);\ \rho\ (m=5) \tag{3}$$

Contrasting the list of variables of Eqs. (1) and (3) allows us to mathematically treat Cases 1 and 2 at the same time by considering problems involving the following set of variables:

$$v;\ a;\ \ell;\ (\mu g);\ \rho \qquad \text{where } \mu = \begin{cases} 1 & \text{gravitational (Case 1)} \\ \mu_s & \text{frictional (Case 2)} \end{cases} \tag{4}$$

For this combined case, the total number of variables is $m=5$. These dimensional variables require three $(n=3)$ *fundamental dimensions* to describe them completely. These dimensions are mass [M], length [L], and time [T].

Since the number of dimensions $n=3$, we can now choose three out of the above five variables to serve as the "primary" variables. This leaves $(m-n)=2$ as the "remaining" or "repeated" variables. Also, there will be two non-dimensional Π groups (Π_1 and Π_2) formed in this case.

All of the above variables are expressed in terms of the three $(n=3)$ fundamental dimensions [M], [L], [T] as

$$v=[\mathrm{LT}^{-1}];\ \ a,\ g=[\mathrm{LT}^{-2}];\ \ \ell=[\mathrm{L}];\ \ \rho=[\mathrm{ML}^{-3}] \tag{5}$$

We now choose $n=3$ "primary" or "repeating" variables. This is quite arbitrary but it is advisable, before choosing them, to consider the physics of the problem. Here, we choose one relating to geometry, another to material and the third to the restoring "gravitational" or "frictional" forces. The primary variables chosen are as follows:

$$\left.\begin{array}{ll} \text{Geometry:} & \ell \\ \text{Gravitation:} & (\mu g) \\ \text{Material:} & \rho \end{array}\right\}\ (n=3) \tag{6}$$

The remaining variables are v and a, and they are $(m-n)=2$ in number. For Case 1, $\mu=1$, while for Case 2, $\mu=\mu_s$ as discussed earlier.

Dimensionless Groups Π_1 and Π_2

Each of these groups is formed by multiplying each of the remaining variables v and a by the product of powers of the "primary" variables ℓ, (μg), and ρ as follows:

$$\Pi_1=\ell^{a_1}(\mu g)^{b_1}\rho^{c_1}v \text{ and } \Pi_2=\ell^{a_2}(\mu g)^{b_2}\rho^{c_2}a \tag{7}$$

Expressing each of the above in terms of the fundamental dimensions of their constituent variables (see Eq. (5)) and recalling that each of the Π_i's are dimensionless (i.e., $[\Pi_i]=\mathrm{M}^0\mathrm{L}^0\mathrm{T}^0$) allows us to obtain a_1, b_1, c_1 and a_2, b_2, c_2:

Dimensionless Group $\Pi_1=\ell^{a_1}(\mu g)^{b_1}\rho^{c_1}v$

$$\mathrm{M}^0\mathrm{L}^0\mathrm{T}^0=[\mathrm{L}]^{a_1}[\mathrm{LT}^{-2}]^{b_1}[\mathrm{ML}^{-3}]^{c_1}[\mathrm{LT}^{-1}]$$

$$\left.\begin{array}{ll} \mathrm{M}^0=[\mathrm{M}]^{c_1} & \Rightarrow c_1=0 \\ \mathrm{L}^0=[\mathrm{L}]^{a_1+b_1-3c_1+1} & \Rightarrow a_1+b_1-3c_1+1=0 \\ \mathrm{T}^0=[\mathrm{T}]^{-2b_1-1} & \Rightarrow -2b_1-1=0 \end{array}\right\} \begin{array}{l} a_1=-\frac{1}{2} \\ b_1=-\frac{1}{2} \\ c_1=0 \end{array}$$

Thus,

$$\Pi_1=\ell^{-1/2}(\mu g)^{-1/2}v=\frac{v}{\sqrt{\ell(\mu g)}} \tag{8}$$

Dimensionless Group $\Pi_2=\ell^{a_2}(\mu g)^{b_2}\rho^{c_2}a$

$$\mathrm{M}^0\mathrm{L}^0\mathrm{T}^0=[\mathrm{L}]^{a_2}[\mathrm{LT}^{-2}]^{b_2}[\mathrm{ML}^{-3}]^{c_2}[\mathrm{LT}^{-2}]$$

$$\left.\begin{array}{ll} \mathrm{M}^0=[\mathrm{M}]^{c_2} & \Rightarrow c_2=0 \\ \mathrm{L}^0=[\mathrm{L}]^{a_2+b_2-3c_2+1} & \Rightarrow a_2+b_2-3c_2+1=0 \\ \mathrm{T}^0=[\mathrm{T}]^{-2b_2-2} & \Rightarrow -2b_2-2=0 \end{array}\right\} \begin{array}{l} a_2=0 \\ b_2=-1 \\ c_2=0 \end{array}$$

Thus,

$$\Pi_2=(\mu g)^{-1}a=\frac{a}{(\mu g)} \tag{9}$$

From Eqs. (8) and (9), one can see that the dynamic problem is now expressible as a function F of the non-dimensional numbers Π_1 and Π_2 as

$$F(\Pi_1;\ \Pi_2)=F\left(\frac{v}{\sqrt{\ell\mu g}};\ \frac{a}{\mu g}\right)=0 \tag{10}$$

It is important to note that the above equation is *independent* of the mass density ρ for both the "gravitational" and "frictional" cases, a fact that has major implications for scaling and similitude of these structures. Mathematically, this arises from the fact that the BPT requires $c_1=c_2=0$ in the above derivation.

2.1 Introducing the μ^N and Other Dimensionless Groups.

The first dimensionless combination in Eq. (10) will from now on be referred to as the "mu-Number," μ^N, and will be defined as

$$\mu^N:=\Pi_1:=\frac{v}{\sqrt{\ell\mu g}}=F_r^N/\sqrt{\mu} \tag{11}$$

The μ-number is a generalization of the "Froude number," $F_r^N:=v/\sqrt{\ell g}$, and has been introduced here to simultaneously account for gravitational restoring forces (when $\mu=1$), and also for "frictional" restoring forces (when $\mu=\mu_s$). Note that when $\mu=1$, the non-dimensional group $\Pi_1=v/\sqrt{\ell\mu g}$ reduces to $v/\sqrt{\ell g}=F_r^N$ while $a/\mu g$ reduces to a/g; thus, the acceleration scales directly with g. Also, given the non-dimensional nature of Eq. (10), one can express v and a in terms of the two non-dimensional groups $\Pi_1(\cdot)$ and $\Pi_2(\cdot)$:

$$v=\sqrt{\ell\mu g}\ \Pi_1\left(\frac{a}{\mu g}\right) \tag{12}$$

and

$$a=\mu g\ \Pi_2\left(\frac{v}{\sqrt{\ell\mu g}}\right)=\mu g\ \Pi_2(\mu^N) \tag{13}$$

where $\Pi_1(\cdot)$ and $\Pi_2(\cdot)$ are unknown functions of the remaining Π groups, i.e., $\Pi_1=\Pi_1(a/\mu g)$ and $\Pi_2=\Pi_2(\mu^N)$.

It should also be noted that here we have decided to represent the dynamics of the rigid system in terms of v and a (see Eq. (4)), not

time. This resulted in two dimensionless numbers Π_1 and Π_2 involving v and a, respectively, whose ratio can be used to obtain a dimensionless number for time t. Alternatively, we could have described the dynamic problem in terms of v and t and not a. In that case, application of the BPT would have resulted in the following dimensionless description of the dynamical problem:

$$F(\Pi_1;\Pi_t)=F\left(\frac{v}{\sqrt{\ell\mu g}};t\sqrt{\frac{\mu g}{\ell}}\right)=0 \tag{14}$$

where $\Pi_1=\mu^N:=v/\sqrt{\ell\mu g}$ and $\Pi_t:=t\sqrt{\mu g/\ell}$.

It should be observed that Eq. (14) is equivalent to Eq. (10) in describing the dynamical problem and that, as expected from dimensional analysis, time is dimensionally given by

$$t=\frac{v}{a}=\sqrt{\frac{\ell}{\mu g}}\,\Pi_t \tag{15}$$

where $\Pi_t=\Pi_1/\Pi_2$.

2.2 μ^N Scaling for Discrete, Rigid Systems. The results of the previous section and, in particular, Eqs. (12) and (13) provide the basis of comparing a model system (M) to a prototype system (P). In these expressions, $\Pi_1(\cdot)$ and $\Pi_2(\cdot)$ are unknown functions of the remaining dimensionless groups. That is, $\Pi_1=\Pi_1(\Pi_2)$ and $\Pi_2=\Pi_2(\Pi_1)$, while Eqs. (12) and (13) are the basic relations which govern "μ^N similitude." Indeed, for complete similitude, or consistency, to be satisfied between a model and a prototype, both $\Pi_1:=\mu^N$ and Π_2 need to be kept equal between the two systems, i.e., $\Pi_1^M=\Pi_1^P$ and $\Pi_2^M=\Pi_2^P$. For such systems, applying Eqs. (12) and (13) to each of the problems and dividing by sides, keeping in mind that Π_1 and Π_2 remain invariant, provides "scaling laws" for the basic independent problem variables v and a. Similarly, Eq. (15) can be used to scale the time variable t.

Velocity Scaling

Applying Eq. (12) to both the model and prototype gives

$$v^M=\sqrt{\ell^M\mu^M g^M}\;\Pi_1^M,\quad v^P=\sqrt{\ell^P\mu^P g^P}\;\Pi_2^P$$

where $\Pi_1^M=\Pi_1^P$ and $\Pi_2^M=\Pi_2^P$, which is equivalent to

$$v^M=v^P\left(\frac{\ell^M}{\ell^P}\right)^{1/2}\left(\frac{\mu^M}{\mu^P}\right)^{1/2}\left(\frac{g^M}{g^P}\right)^{1/2} \tag{16}$$

Acceleration Scaling

Applying Eq. (13) to both model and prototype gives

$$a^M=a^P\left(\frac{\mu^M}{\mu^P}\right)\left(\frac{g^M}{g^P}\right) \tag{17}$$

Time Scaling

Applying Eq. (15) to both model and prototype gives

$$t^M=t^P\left(\frac{\ell^M}{\ell^P}\right)^{1/2}\left(\frac{\mu^P}{\mu^M}\right)^{1/2}\left(\frac{g^P}{g^M}\right)^{1/2} \tag{18}$$

The above scaling laws Eqs. (16)–(18) result from the enforcement of μ^N similitude (i.e., keeping the $\mu^N=v/\sqrt{\ell\mu g}$ number as well as $\Pi_2=a/\mu g$ constant between model and prototype). It will be referred to here as "μ^N scaling." For MTS model/prototype pairs of the type depicted in Fig. 2(*b*), Eqs. (16) and (18) furnish the appropriate ground velocity and time scaling provided that the constituent blocks are strictly rigid and that the inter-block restoring forces are primarily gravitational/frictional as will be discussed in a following section.

2.3 Consequences of μ^N Scaling. The scaling relations Eqs. (16)–(18) exhibit some remarkable properties when applied to either Case 1 (pure rocking) or Case 2 (frictional sliding and frictional rock/sliding) or, under certain circumstances, for a mixture of the two. These properties are summarized below:

A. When μ^N similitude is enforced, *density*, and thus *mass*, is *not involved* in velocity, acceleration, and time scaling. This implies that no additional mass needs to be added to the model system to achieve similitude. This holds for both Cases 1 and 2 considered thus far.

B. For model/prototype systems with the same non-zero coefficient of friction $\mu_s^M=\mu_s^P$ (or $\mu^M=\mu^P$) for both Cases 1 and 2, μ^N scaling of Eqs. (16)–(18) reduces to

$$\begin{aligned}v^M&=v^P\left(\frac{\ell^M}{\ell^P}\right)^{1/2}\left(\frac{g^M}{g^P}\right)^{1/2}\\ a^M&=a^P\left(\frac{g^M}{g^P}\right)\\ t^M&=t^P\left(\frac{\ell^M}{\ell^P}\right)^{1/2}\left(\frac{g^P}{g^M}\right)^{1/2}\end{aligned} \tag{19}$$

and is identical for both Cases 1 and 2. If further, the model and prototype are in the same gravitational environment ($g^P=g^M$), then

$$v^M=v^P\sqrt{\lambda_\ell},\quad a^M=a^P,\quad t^M=t^P\sqrt{\lambda_\ell} \tag{20}$$

where $\lambda_\ell=\ell^M/\ell^P$. It is observed at this point that for purely gravitational, frictionless systems (Case 1) experiencing only rocking of the blocks with no sliding ($\mu=1$), μ^N scaling is equivalent to F_r^N scaling since $\mu^N=F_r^N$. Remarkably, this conclusion also holds even for frictional systems where $\mu^N\neq F_r^N$ provided that the model has the same coefficient of friction as the prototype ($\mu_s^M=\mu_s^P$). The above observations naturally imply that μ^N scaling is also applicable for "mixed systems" involving some parts which experience rocking, some parts that experience pure sliding and some parts which experience a mixture of sliding and rocking, provided again that the friction coefficients of the model and prototype are the same. This is a powerful conclusion since most incoherently (frictionally) held block systems indeed involve all of these physical mechanisms (i.e., rocking; sliding; rock/sliding shown in Fig. 3) when subjected to strong dynamic base excitations often involving substantial ground-vertical components. Finally for such systems, despite the fact that μ^N does not reduce to F_r^N, the scaling relations of Eqs. (19)–(20) obtained on the basis of μ^N and F_r^N similitude become identical when $\mu_s^M=\mu_s^P$.

C. For mainly frictional model/prototype systems (involving sliding and frictional rocking), which do not have the same friction coefficient ($\mu_s^P\neq\mu_s^M$), and for systems and excitations where the structure mainly experiences sliding and frictional dissipation (Case 2), Eqs. (16)–(18) are applicable with $\mu=\mu_s$, and the μ^N number defined in Eq. (11) is the only appropriate non-dimensional quantity. If further $g^M=g^P$, then the μ^N scaling gives

$$\begin{aligned}v^M&=v^P\left(\frac{\ell^M\mu_s^M}{\ell^P\mu_s^P}\right)^{1/2}=v^P\sqrt{\lambda_\ell\lambda_\mu}\\ a^M&=a^P\left(\frac{\mu_s^M}{\mu_s^P}\right)=a^P\lambda_\mu\\ t^M&=t^P\left(\frac{\ell^M\mu_s^P}{\ell^P\mu_s^M}\right)^{1/2}=t^P\sqrt{\frac{\lambda_\ell}{\lambda_\mu}}\end{aligned} \tag{21}$$

where $\lambda_\ell=\ell^M/\ell^P$ and $\lambda_\mu=\mu_s^M/\mu_s^P$. This is called μ^N scaling for the same gravity environment.

D. μ^N scaling is useful when the two systems (model/prototype) have different friction coefficients. Since it also involves

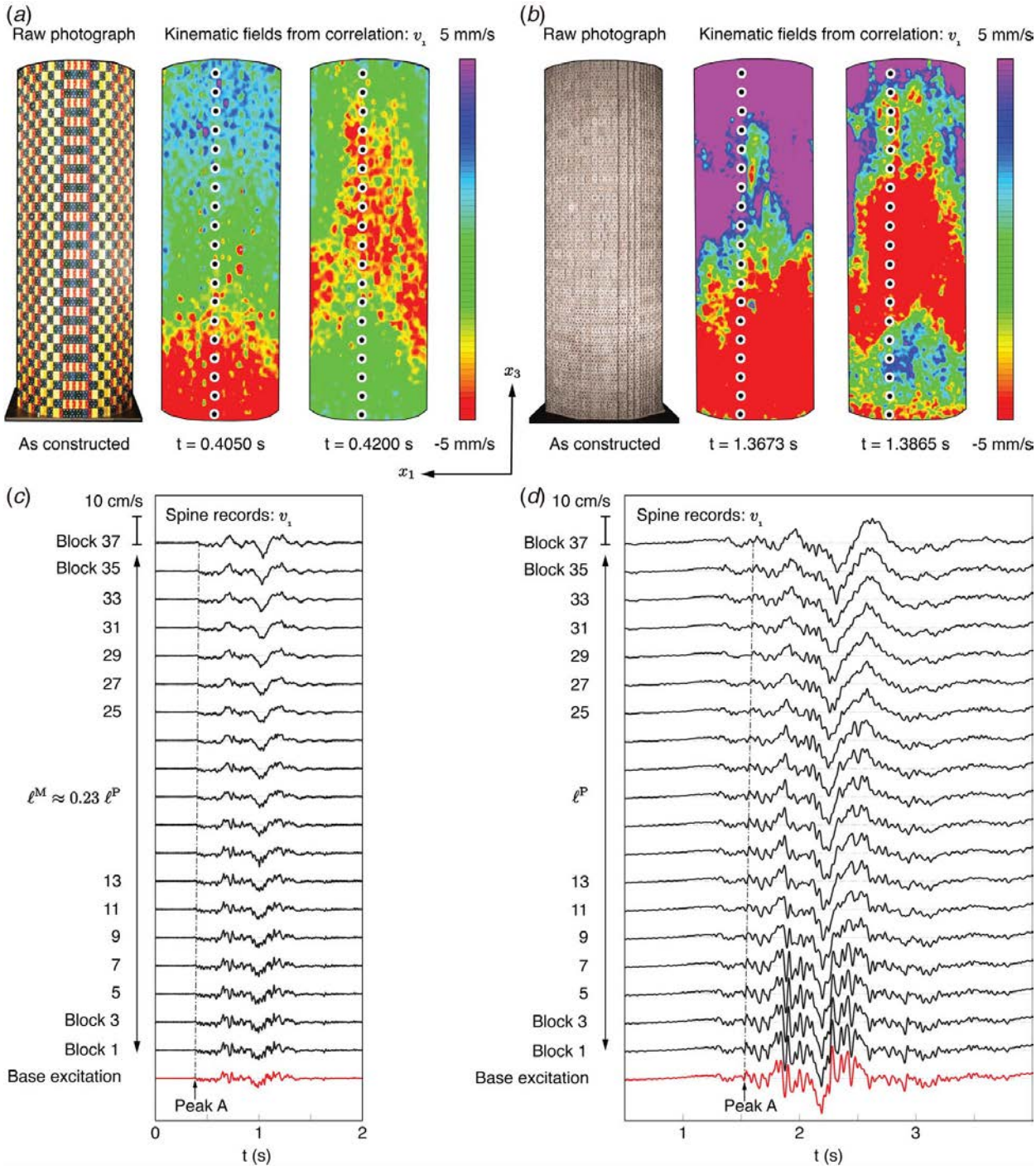

Fig. 4 High-speed optical measurements of the horizontal velocity component v_1 (color plots), enabled by digital image correlation (DIC) for (*a*) an aluminum (Al) and (*b*) concrete model/prototype tower pair. Panels (c) and (*d*) show velocity time histories of the imposed, scaled base excitations (red), and the resulting velocities (black) of individual blocks situated at 19 points (circles) up the heights of the 38 story towers. These histories are called the "spine records." It should be noted that the length and mass of the model Al and prototype concrete towers are $\ell^M = 1.51$ m, $\ell^P = 6.46$ m, and $m^M = 255$ kg, $m^P = 14{,}930$ kg, respectively.

$\lambda_\mu = \mu_s^M/\mu_s^P$, which appropriately multiplies λ_ℓ in Eq. (21), it provides an additional lever allowing the modeler to choose more realistic length scale ratios in order to achieve similitude between a "small-scale" experimental model structure and a "full-scale" prototype. The experiments presented in Fig. 4 which involve geometrically similar aluminum/concrete systems at two different length scales represent such a case of two systems involving very different coefficients of friction. Here, scaling is provided by Eq. (21).

E. When different gravity environments are considered (e.g., Planetary versus Earth gravity; artificial gravity in rotating systems at the lab or space), μ^N scaling provides flexibility in choosing model gravitational conditions as well as various coefficients of friction and length scales.

2.4 Properties and Physical Interpretation of μ^N. The sections above introduce a new non-dimensional number μ^N and discuss its significance in scaling of both gravitational and frictional

rigid body systems. In particular, we have introduced the notion of μ^N similitude and have first proposed that it can be used for scaling rigid body model/prototype systems featuring different coefficients of friction and gravitational environments, provided they involve frictional sliding (sliding/rock-sliding) as their major dynamic deformation mechanism. Also, we have found that the invariance of μ^N can also provide scaling for all model/prototype systems of identical friction coefficient, even if such systems involve mixed deformation mechanisms with some parts experiencing rocking, some pure sliding and some a mixture of frictional sliding and frictional rocking. Indeed, when in addition the model/prototype pairs are subjected to the same gravitational environment, then the resulting relations reduce to classical Froude scaling even if friction remains the dominant mechanism, provided, of course, that $\mu_s^M = \mu_s^P$ and $g^M = g^P$. To further clarify these results, we observe that the μ^N number can be interpreted in terms of ratios of "driving" and "restoring" force densities as follows:

$$\mu^N := \left(\frac{v}{\sqrt{\mu \ell g}}\right) = \left(\frac{\rho v^2}{\rho \mu \ell g}\right)^{1/2} = \left(\frac{\rho a}{\mu \rho g}\right)^{1/2} = \left(\frac{f_i}{f_r}\right)^{1/2} \tag{22}$$

where $f_i = \rho a$ is the driving *inertial* force density and $f_r = \mu \rho g$ is the *restoring* (or *resisting*) force density.

When $\mu = 1, f_r = \rho g = f_g$ becomes a purely *gravitational restoring force density*. Furthermore, μ^N reduces to F_r^N. However, when $\mu = \mu_s$, $f_r = \mu_s \rho g = f_f$ becomes the *frictional restoring force density*. Motivated by the physical interpretation of the dimensionless number μ^N as the ratio of inertial to resisting force densities, we will subsequently explore the implications of applying the BPT to rigid body systems involving arbitrary restoring force densities f_r acting at the interfaces between the rigid particles or blocks.

3 Rigid Body Systems Involving Various Types of "Restoring" Force Densities (Case 3)

Here, in addition to the kinematic variables v and a, length ℓ, and material mass density ρ, we choose to separately list the restoring force density, f_r, as a system variable. This is an alternative choice of variables motivated by the interpretation of μ^N as a ratio of inertial force to restoring force densities, which suggests the possibility of generalization to arbitrary restoring forces. After the appropriate Π groups are generally established in terms of f_r, we introduce an arbitrary "restoring force" dimensionless number R_F^N. We then specialize the results for the interfacial force densities f_r being "gravitational," "frictional," and "cohesive." These are only a few examples of the many types of restoring forces possible in such systems. The blocks are assumed to be rigid in all cases and elastic properties are not explicitly stated in the list of variables. Here, the general list of variables is

$$v;\ a;\ \ell;\ \rho;\ f_r \quad (m = 5) \tag{23}$$

Each of the above variables involve the following groups of fundamental dimensions:

$$v = [\mathrm{LT}^{-1}];\ \ a = [\mathrm{LT}^{-2}];\ \ \ell = [\mathrm{L}]$$
$$\rho = [\mathrm{ML}^{-3}];\ \ f_r = [\mathrm{ML}^{-2}\mathrm{T}^{-2}]$$

We now choose the following primary variables which is a generalization of our earlier choice of these variables as they appear in Eq. (6):

$$\left.\begin{array}{ll} \text{Geometry:} & \ell \\ \text{Restoring force density:} & f_r \\ \text{Material:} & \rho \end{array}\right\} \ (n = 3) \tag{24}$$

The remaining two variables are v and a, and as a result, we have $(m - n) = 2$ dimensionless Π groups as follows:

$$\Pi_1 = \ell^{a_1} \rho^{b_1} f_r^{c_1} v;\ \ \Pi_2 = \ell^{a_2} \rho^{b_2} f_r^{c_2} a$$

Solving for the coefficients above results in the dimensionless groups $\Pi_1 = v/\sqrt{\rho/f_r \ell}$ and $\Pi_2 = \rho a / f_r$. The system is now expressible as

$$f(\Pi_1; \Pi_2) = f\left(v\sqrt{\frac{\rho}{f_r \ell}};\ \frac{\rho a}{f_r}\right) = 0 \tag{25}$$

It should be noted that for arbitrary restoring forces densities, the mass density ρ reappears in the dimensionless numbers. We later see that ρ only disappears for specific forms of f_r.

3.1 Introducing the "Arbitrary Restoring Force" Dimensionless Number R_F^N. Motivated by the form of Eq. (25), we identify the Π_1 dimensionless group as an important quantity governing similitude in Case 3 discussed earlier. We consequently define a general dimensionless number R_F^N as

$$R_F^N := \Pi_1 := v\sqrt{\frac{\rho}{f_r \ell}} \tag{26}$$

and call it the "Arbitrary Restoring Force Number," R_F^N. It should be noted that R_F^N can be expressed as

$$R_F^N = \frac{v}{\sqrt{f_r \ell/\rho}} = \left(\frac{\rho v^2}{f_r}\right)^{1/2} = \left(\frac{\rho a}{f_r}\right)^{1/2} = \left(\frac{f_i}{f_r}\right)^{1/2} \tag{27}$$

and can thus be directly interpreted in terms of ratios of "inertial" ρa and arbitrary "restoring" force densities f_r of various types. R_F^N is a general dimensionless number which naturally arises as a consequence of the application of the BPT methodology. Indeed, comparison of Eq. (27) with Eq. (22) suggests that R_F^N is a generalization of the μ^N and F_r^N numbers discussed above for systems involving frictional or gravitational restoring forces, respectively. As we will see in Sec. 4 where intra-block elasticity is included, R_F^N reduces to the Cauchy number C^N, provided that the restoring forces are elastic.

We now consider various types of "restoring" force densities f_r and explore the resulting forms of R_F^N and the specialized types of similitude for each case.

3.1.1 Gravitational Restoring Force Densities. Then, $f_r = f_g = \rho g$ and Eqs. (25) and (26) give

$$R_F^N := \Pi_1 := v\sqrt{\frac{\rho}{(\rho g)\ell}} = \frac{v}{\sqrt{\ell g}} = F_r^N$$
$$\Pi_2 = \frac{\rho a}{\rho g} = \frac{a}{g}$$

Also note that here $R_F^N = F_r^N$ and Eq. (25) reduces to

$$f(\Pi_1; \Pi_2) = f\left(\frac{v}{\sqrt{\ell g}};\ \frac{a}{g}\right) = f\left(F_r^N;\ \frac{a}{g}\right) = 0 \tag{28}$$

3.1.2 Frictional Restoring Force Densities. Then, $f_r = f_f = \rho \mu_s g$ and Eqs. (25) and (26) give

$$R_F^N := \Pi_1 := \frac{v}{\sqrt{\mu_s \ell g}} = \frac{F_r^N}{\sqrt{\mu_s}} = \mu^N$$
$$\Pi_2 = \frac{a}{\mu_s g}$$

In this case, $R_F^N = \mu^N$ and the system becomes

$$f(\Pi_1; \Pi_2) = f\left(\frac{v}{\sqrt{\mu_s \ell g}};\ \frac{a}{\mu_s g}\right) = 0 \tag{29}$$

as in Eq. (10) for $\mu = \mu_s$.

3.1.3 Both Gravitational and Frictional Restoring Force Densities. If $f_r = \rho \mu g$, again $R_F^N = \mu^N$ with $\mu = 1$ for the gravitational case and $\mu = \mu_s$ for the frictional case, then

$$R_F^N := \Pi_1 = \frac{v}{\sqrt{\mu \ell g}}, \quad \Pi_2 = \frac{a}{\mu g}$$

while

$$f(\Pi_1; \Pi_2) = f\left(\frac{v}{\sqrt{\mu \ell g}}; \frac{a}{\mu g}\right) = f\left(\mu^N; \frac{a}{\mu g}\right) = 0 \tag{30}$$

Equation (30) covers both Cases 1 and 2 and is identical to Eq. (10) obtained by a less general methodology, which is recovered here as a special case.

3.1.4 Cohesive Restoring Force Density. In a system of characteristic length ℓ, area $A = \ell^2$, and volume $V = \ell^3$ and if the inter-block restoring forces F arise from a constant critical cohesive stress $\sigma = \tau_0$ (cohesive strength), then the restoring force density will be dimensionally given by $f_r = F/V = (\sigma \ell^2)/\ell^3 = \tau_0/\ell$. In such a system, τ_0 is assumed to be independent of weight or normal stress and in practice may be due to the "constant strength" of interfacial mortar in masonry or to a constant "yield strength" when the inter-block resistance is provided by highly ductile (rigid-plastic) metal joints. In this case, Eqs. (25) and (27) give

$$R_F^N := \Pi_1 = v\sqrt{\frac{\rho}{(\tau_0/\ell)\ell}} = v\sqrt{\frac{\rho}{\tau_0}}$$

$$\Pi_2 = \frac{\ell \rho a}{\tau_0}$$

Here, R_F^N reduces to $v\sqrt{\rho/\tau_0}$. This number is the dimensionless combination governing kinematic and time similitude when the restoring forces are cohesive and will be called the "Cohesive Strength Number," S^N. Also, Eq. (25) becomes

$$g(\Pi_1; \Pi_2) = g\left(v\sqrt{\frac{\rho}{\tau_0}}; \frac{\ell \rho a}{\tau_0}\right) = g\left(S^N; \frac{\ell \rho a}{\tau_0}\right) = 0 \tag{31}$$

The last dimensionless group in Eq. (31) represents the scaling of inter-block strength for this gravity load structure, i.e., $\tau_0 = \ell \rho g \Pi_3$. Finally, the new dimensionless "Cohesive Strength Number" S^N governing similitude is defined as

$$S^N := v\sqrt{\frac{\rho}{\tau_0}} \tag{32}$$

3.2 Observations

A. In Cases 1 and 2 where $f_r = \mu \rho g$ with $\mu = 1$ or $\mu = \mu_s$, respectively, $R_F^N = \mu^N$ and the system performance becomes independent of the mass density while the dynamics of the system scale with μ^N and $a/\mu g$.
B. When the restoring force density is provided by a constant cohesive strength, then R_F^N reduces to the "Cohesive Strength Number" $S^N := v\sqrt{\rho/\tau_o}$. The mass density re-enters the system and plays a role in similitude through the ratio τ_0/ρ.
C. Points A and B above explain the difference in satisfying similitude between traditional "masonry" model/prototype structures involving cohesion (mortar) between building blocks and achieving the same for "frictionally held" structures or "soil structures" where gravity and Coulomb-like interfacial strength laws are of relevance.

4 General Discrete Systems (Including Intra-Block or Inter-Block Elasticity) Involving Various Types of "Restoring" Force Densities (Case 4)

Here, we adopt the methodology of Sec. 3 where our system variables include an arbitrary restoring force density f_r (force/unit volume) acting between the discrete blocks, but we also explicitly add individual block elasticity (intra-block elasticity) by explicitly including elastic modulus E or an equivalent spring stiffness to the list of variables. In this case, the list of variables becomes

$$v; a; \ell; \rho; f_r; E \ (m = 6) \tag{33}$$

Each of the above variables involves the following groups of the $(n = 3)$ fundamental dimensions [M], [L], and [T] as: $v = [LT^{-1}]$; $a = [LT^{-2}]$; $\ell = [L]$; $\rho = [ML^{-2}]$; $f_r = [ML^{-2}T^{-2}]$; $E = [ML^{-1}T^{-2}]$.

We choose the following primary variables:

$$\left.\begin{array}{ll} \text{Geometry:} & \ell \\ \text{Restoring force density:} & f_r \\ \text{Material:} & \rho \end{array}\right\} \ (n = 3)$$

The remaining $(m - n) = 3$ variables are v, a, and E. In this case, we have three dimensionless Π groups:

$$\Pi_1 = \ell^{a_1} \rho^{b_1} f_r^{c_1} v; \quad \Pi_2 = \ell^{a_2} \rho^{b_2} f_r^{c_2} a; \quad \Pi_3 = \ell^{a_4} \rho^{b_4} f_r^{c_4} E$$

The expressions for Π_1 and Π_2 above are exactly the same as in the case discussed in Sec. 3 (Eq. (25)), given by

$$\Pi_1 = v\left(\frac{\rho}{f_r \ell}\right)^{1/2}, \quad \Pi_2 = \frac{\rho a}{f_r} \tag{34}$$

However, the difference here to the case of Sec. 3 will become apparent when Π_3 is calculated. To obtain Π_3, we express it in terms of fundamental variables [M], [L], and [T]:

$$M^0 L^0 T^0 = [L]^{a_4} [ML^{-3}]^{b_4} [ML^{-2}T^{-2}]^{c_4} [ML^{-1}T^{-2}]$$

which gives $a_4 = 1$, $b_4 = 0$, and $c_4 = 1$, thus

$$\Pi_3 = \frac{E}{\ell f_r} \tag{35}$$

As a result of the above, the system is described as a function $f(\cdot;\cdot;\cdot)$ of the three dimensionless groups as

$$f(\Pi_1; \Pi_2; \Pi_3) = f\left(v\sqrt{\frac{\rho}{f_r \ell}}; \frac{\rho a}{f_r}; \frac{E}{\ell f_r}\right) = 0 \tag{36}$$

Equation (36) is the most general expression describing a discrete system and featuring an arbitrary restoring force density f_r. The group Π_1 can again be identified as the arbitrary restoring force dimensionless number R_F^N defined in Sec. 3.1 (Eq. (26)).

The presence of the third dimensionless number, $\Pi_3 = E/\ell f_r$, is a direct consequence of including the variable E in the list of problem variables (Eq. (33)), even if the interfacial restoring force is inelastic. By introducing a one-dimensional wave speed $c = \sqrt{E/\rho}$, this number reduces to $\Pi_3 = \rho c^2/\ell f_r$ and reflects the existence of elastic waves in the system. If one compares Eq. (36) with Eq. (25) of Sec. 3, which was derived for a strictly rigid system in the absence of elasticity, it is found that they share the first two dimensionless groups with the third one missing in Eq. (25). This is not surprising since the analysis leading to Eq. (36) is a generalization of the rigid block case. As a result, the third dimensionless group provides an additional constraint that will have to be satisfied in order to fully satisfy similitude between model/prototype systems in the presence of elasticity, even in cases when the restoring forces f_r between the blocks are kept arbitrary.

It should further be noted that in discrete element models such as LS-DEM [32] where the system elasticity is represented by an equivalent elastic spring stiffness, K, even in the presence of arbitrary restoring force f_r at the block interfaces, the list of variables equivalent to those in Eq. (33) will be v; a; ℓ; ρ; f_r; K. In such systems application of the BPT methodology yields a dimensionless dynamical system representation of the form

$$f\left(v\sqrt{\frac{\rho}{f_r \ell}}; \frac{\rho a}{f_r}; \frac{K}{\ell^2 f_r}\right) = 0 \tag{37}$$

Not surprisingly, the first two dimensionless groups in Eq. (37) are identical to those of Eq. (36). Furthermore, the third dimensionless group $\Pi_3 = K/\ell^2 f_r$ in Eq. (37) reduces to $\Pi_3 = E/\ell f_r = \rho c^2/\ell f_r$, as it appears in Eq. (36), if one observes that K and E are related by $E = K/\ell$ through dimensional analysis, demonstrating the complete equivalence of representing elasticity either in terms of a modulus E or a spring stiffness K.

In the following sections, we specialize the general system described in Eq. (36) or (37) to various types of restoring force densities acting between the blocks of the discrete system and then explore their individual characteristics.

4.1 Purely Elastic Restoring Force. If the system is purely elastic, the restoring force per unit volume is also elastic and is given by $f_r = (\sigma A)/V = \sigma/\ell = (E\epsilon)/\ell$ and, since the strain ϵ is non-dimensional, $f_r = E/\ell$ and the Π groups in Eq. (36) become

$$R_F^N := \Pi_1 = v\sqrt{\frac{\rho}{E}} = \frac{v}{c}$$

$$\Pi_2 = \ell\rho a/E = \ell a/c^2, \quad \Pi_3 = 1$$

where $c = \sqrt{E/\rho}$ is the system's bar wave speed. The system is now described as

$$\tilde{f}\left(\frac{v}{c}; \frac{\ell a}{c^2}\right) = 0 \tag{38}$$

where $C^N := v/c$ is the "Cauchy Number." In this case, $R_F^N = C^N$ and the system obeys the classical Cauchy number similitude law which is known to govern similitude in purely elastic systems [7,8]. For models where elasticity is represented by a spring stiffness K, such as LS-DEM [32], and for the special case when the inter-block restoring forces F are also purely elastic, $F = K/\ell$ and the restoring force per unit volume becomes $f_r := F/\ell^3 = K/\ell^2$. In this case, the system is described by

$$g\left(v\sqrt{\frac{\rho\ell}{K}}; \frac{\rho a \ell^2}{K}\right) = 0 \tag{39}$$

Comparing Eq. (39) to Eq. (38) and recalling that dimensionally $K = E\ell$ and $c^2 = E/\rho$, one observes that they become identical. This demonstrates the equivalence of representing system elasticity either by bulk elastic properties such as E, or by spring stiffness such as K. Furthermore, Cauchy similitude holds for both cases.

4.2 Constant Cohesive Strength Force Density. If the restoring force density is cohesive (i.e., $f_r = \tau_0/\ell$), where τ_0 is a constant cohesive strength independent of weight, then R_F^N reduces to the strength number $S^N := v\sqrt{\rho/\tau_0}$ and the dimensionless Π groups in Eq. (36) become

$$R_F^N := \Pi_1 = v\sqrt{\frac{\rho}{\tau_0}} = S^N$$

$$\Pi_2 = \frac{\ell\rho a}{\tau_0}, \quad \Pi_3 = \frac{E}{\tau_0}$$

while the system is described by

$$\hat{g}\left(v\sqrt{\frac{\rho}{\tau_0}}; \frac{\ell\rho a}{\tau_0}; \frac{E}{\tau_0}\right) = 0 \tag{40}$$

4.3 Gravitational/Frictional System With Intra-Block or Inter-Block Spring Elasticity. If the system is gravitational and/or frictional (i.e., $f_r = \rho\mu g$), then $R_F^N = \mu^N$ and the dimensionless Π groups of Eq. (36) or (37) become

$$R_F^N := \Pi_1 = \frac{v}{\sqrt{\ell\mu g}} = \mu^N$$

$$\Pi_2 = \frac{a}{\mu g}; \quad \Pi_3 = \frac{c^2}{\ell\mu g} \left(\text{or } \Pi_3 = \frac{K}{\ell^2\mu\rho g}\right)$$

The system is now described by

$$\tilde{g}\left(\frac{v}{\sqrt{\ell\mu g}}; \frac{a}{\mu g}; \frac{c^2}{\ell\mu g}\right) = 0 \tag{41}$$

or

$$\tilde{g}\left(\frac{v}{\sqrt{\ell\mu g}}; \frac{a}{\mu g}; \frac{K}{\ell^2\mu\rho g}\right) = 0 \tag{42}$$

for gravitational/frictional systems described by LS-DEM types of models, where elasticity is represented in terms of spring stiffness K.

4.4 Discussion and Summary of Results. Equations (36)–(42) provide the various forms of system behavior and dimensionless groups that arise from the most general case of a discrete system of elastic blocks featuring various types of elastic or dissipative (inelastic) restoring force densities at their interfaces.

A common characteristic in all of the cases discussed above is the appearance of the dimensionless number $\Pi_3 = E/\ell f_r = \rho c^2/\ell f_r$ in Eq. (36) and in all its special cases with the exception of the elastic case where Π_3 becomes trivial ($\Pi_3 = 1$). This number appears because of the addition of the elastic modulus E in the list of problem variables (Eq. (33)) even when the restoring forces are purely inelastic. It reflects the existence of elastic waves in the system and as such it is absent in Cases 1–3 (Secs. 2 and 3) where the more idealized problem of perfectly rigid blocks is initially considered.

Each of the choices for f_r presented here show that kinematic quantities, such as velocities and accelerations, appear in various dimensionless groups which reveal the many different types of scaling laws that need to be observed in order to ensure similitude between model and prototype systems in each of these cases. In particular, we have defined here a variety of dimensionless groups: $R_F^N := v\sqrt{\rho/f_r\ell}$ (arbitrary restoring force number), $\mu^N := v/\sqrt{\ell\mu g}$ (μ-number), $F_r^N := v/\sqrt{\ell g}$ (Froude number), $C^N := v/\sqrt{\rho/E} = v/c$ (Cauchy number) and $S^N := v/\sqrt{\rho/\tau_0}$ (cohesive strength number) which are appropriate to each of the general, gravitational/frictional, elastic and cohesive strength restoring force densities, respectively. Unlike the perfectly rigid block case, the elastic constants and density (or wave speeds) also need to scale through the presence of the third dimensionless group Π_3, which provides the necessary material property scaling between a model/prototype system.

For models such as LS-DEM [31] where the system elasticity is represented by a spring stiffness K instead of an elastic modulus E, even if the restoring force f_r remains arbitrary, this group reduces to $\Pi_3 = K/\ell^2 f_r$ and provides the necessary stiffness scaling for the spring constants involved in these models.

In what follows, we will refer to the combination on the scaling requirements provided by the dimensionless group $\Pi_3 = \rho c^2/\ell f_r$ (or $K/\ell^2 f_r$) in addition to the dimensionless numbers discussed above as complete R_F^N, μ^N, F_r^N, C^N, or S^N similitudes, respectively. For each of these cases, there are specific scaling relations that need to be satisfied in order to ensure complete similitude between a model and a prototype. These will be detailed in Sec. 5.

5 General Forms of Scaling Relations for Discrete Systems Obeying Similitude

The dimensional analysis for the general case of discrete systems of elastic blocks including various types of restoring force densities f_r has resulted in a dimensionless problem description of the form

described in Sec. 4, Eqs. (36) and (37). The dimensionless groups Π_1 to Π_3 involved in these equations provide the basis of comparing the behavior of a model system (M) to a prototype system (P), provided that these two systems are chosen in such a way as to obey similitude. Indeed, obeying similitude means that all of the dimensionless quantities involving the independent system variables must remain invariant between model and prototype. Such systems are called "similar," and their variables are connected by specific scaling relations which we will describe in this section. Time t and other dependent variables can also easily be added to the list, since they can be calculated via simple dimensional analysis from the known dimensionless groups involving our chosen independent variables. In particular, here we also choose to provide the dimensionless groups and scaling relations for the angular velocity $\dot{\theta}$ and the angular acceleration $\ddot{\theta}$, since these are important experimentally measured quantities in discrete systems, especially those involving rocking. These additional variables can be expressed as

$$t = \sqrt{\frac{\rho \ell}{f_r}}\Pi_t, \quad \dot{\theta} = \sqrt{\frac{f_r}{\ell \rho}}\Pi_{\dot{\theta}}, \quad \ddot{\theta} = \frac{\ell \rho}{f_r}\Pi_{\ddot{\theta}}$$

where $\Pi_t = \Pi_1/\Pi_2$, $\Pi_{\dot{\theta}} = \Pi_t^{-1}$, and $\Pi_{\ddot{\theta}} = \Pi_t^{-2}$.

Indeed, by expressing each of the problem variables in terms of the dimensionless groups for both model and prototype, recalling that all dimensionless groups must remain invariant for similitude to be satisfied ($\Pi_i^M = \Pi_i^P$) and dividing by sides, one obtains scaling relations for each of the kinematic variables, time, and wave speeds. These are described in detail in the sections that follow for various types of restoring forces densities.

5.1 General Scaling Relations ($R_F^N := v V \sqrt{\rho/f_r \ell}$ Similitude). When the restoring force density f_r is left arbitrary or unspecified, and if in addition, we include the effect of different gravitational environments between the model and the prototype ($g^M \neq g^P$), the scaling relations become

$$\begin{aligned}
v^M &= v^P \left(\frac{\ell^M}{\ell^P}\right)^{1/2} \left(\frac{f_r^M}{f_r^P}\right)^{1/2} \left(\frac{\rho^P}{\rho^M}\right)^{1/2} \\
a^M &= a^P \left(\frac{f_r^M}{f_r^P}\right) \left(\frac{\rho^P}{\rho^M}\right) \\
t^M &= t^P \left(\frac{\ell^M}{\ell^P}\right)^{1/2} \left(\frac{f_r^P}{f_r^M}\right)^{1/2} \left(\frac{\rho^M}{\rho^P}\right)^{1/2} \\
\dot{\theta}^M &= \dot{\theta}^P \left(\frac{\ell^P}{\ell^M}\right)^{1/2} \left(\frac{f_r^M}{f_r^P}\right)^{1/2} \left(\frac{\rho^P}{\rho^M}\right)^{1/2} \\
\ddot{\theta}^M &= \ddot{\theta}^P \left(\frac{\ell^P}{\ell^M}\right) \left(\frac{f_r^M}{f_r^P}\right) \left(\frac{\rho^P}{\rho^M}\right) \\
c^M &= c^P \left(\frac{\ell^M}{\ell^P}\right)^{1/2} \left(\frac{f_r^M}{f_r^P}\right)^{1/2} \left(\frac{\rho^P}{\rho^M}\right)^{1/2} \quad \text{or} \\
K^M &= K^P \left(\frac{\ell^M}{\ell^P}\right)^2 \left(\frac{f_r^M}{f_r^P}\right)
\end{aligned} \tag{43}$$

5.2 Specialization of Scaling Laws to Various Types of Restoring Force Densities. Here, we consider some simple examples describing the restoring force densities f_r and present the scaling relations appropriate for each case:

Gravitational/Frictional Restoring Force Densities ($\mu^N := v/\sqrt{\ell \mu g}$ Similitude)

In these cases $f_r = \rho \mu g$, where $\mu = 1$ for gravitational and $\mu = \mu_s$ for frictional systems, while the restoring force dimensionless number R_F^N now reduces to μ^N. By substituting in Eq. (43), one gets the following specialization of the scaling relations:

$$\begin{aligned}
v^M &= v^P \left(\frac{\ell^M}{\ell^P}\right)^{1/2} \left(\frac{\mu^M}{\mu^P}\right)^{1/2} \left(\frac{g^M}{g^P}\right)^{1/2} \\
a^M &= a^P \left(\frac{\mu^N}{\mu^P}\right) \left(\frac{g^M}{g^P}\right) \\
t^M &= t^P \left(\frac{\ell^M}{\ell^P}\right)^{1/2} \left(\frac{\mu^P}{\mu^M}\right)^{1/2} \left(\frac{g^P}{g^M}\right)^{1/2} \\
\dot{\theta}^M &= \dot{\theta}^P \left(\frac{\ell^P}{\ell^M}\right)^{1/2} \left(\frac{\mu^M}{\mu^P}\right)^{1/2} \left(\frac{g^M}{g^P}\right)^{1/2} \\
\ddot{\theta}^M &= \ddot{\theta}^P \left(\frac{\ell^P}{\ell^M}\right) \left(\frac{\mu^M}{\mu^P}\right) \left(\frac{g^M}{g^P}\right)^{1/2} \\
c^M &= c^P \left(\frac{\ell^M}{\ell^P}\right)^{1/2} \left(\frac{\mu^M}{\mu^P}\right)^{1/2} \left(\frac{g^M}{g^P}\right)^{1/2} \quad \text{or} \\
K^M &= K^P \left(\frac{\ell^M}{\ell^P}\right)^2 \left(\frac{\mu^M}{\mu^P}\right)^{1/2} \left(\frac{\rho^M}{\rho^P}\right)^{1/2} \left(\frac{g^M}{g^P}\right)^{1/2}
\end{aligned} \tag{44}$$

The first five of the above equations are consistent with μ^N (μ-number) scaling, as discussed in Sec. 2.2, and are independent of density ρ. They only depend on length and on the product μg. The sixth equation, however, represents the effect of elasticity and unlike the rigid case, provides additional constraints on the ratios of wave speeds or stiffnesses for complete similitude to be satisfied when system elasticity is present either through the elastic modulus E or through the spring stiffness K of the structure as discussed in Sec. 4.4, and also introduces a dependence on density ρ.

Elastic Restoring Force Density ($C^N := v/c$ Similitude)

In this case, $f_r = \sigma/\ell = E\epsilon/\ell$, where E is a modulus, σ is a characteristic stress (normal or shear), and ϵ is a dimensionless strain measure. Thus, in a dimensional setting, $f_r = E/\ell$ is used to substitute in Eq. (43) above to give

$$\begin{aligned}
v^M &= v^P \left(\frac{E^M}{E^P}\right)^{1/2} \left(\frac{\rho^P}{\rho^M}\right)^{1/2} = v^P \left(\frac{c^M}{c^P}\right) \\
a^M &= a^P \left(\frac{E^M}{E^P}\right) \left(\frac{\rho^P}{\rho^M}\right) \left(\frac{\ell^P}{\ell^M}\right) = a^P \left(\frac{c^M}{c^P}\right)^2 \left(\frac{\ell^P}{\ell^M}\right) \\
t^M &= t^P \left(\frac{\ell^M}{\ell^P}\right) \left(\frac{E^P}{E^M}\right)^{1/2} \left(\frac{\rho^M}{\rho^P}\right)^{1/2} = t^P \left(\frac{\ell^M}{\ell^P}\right) \left(\frac{c^P}{c^M}\right) \\
\dot{\theta}^M &= \dot{\theta}^P \left(\frac{\ell^P}{\ell^M}\right) \left(\frac{E^M}{E^P}\right)^{1/2} \left(\frac{\rho^P}{\rho^M}\right)^{1/2} = \dot{\theta}^P \left(\frac{\ell^P}{\ell^M}\right) \left(\frac{c^M}{c^P}\right) \\
\ddot{\theta}^M &= \ddot{\theta}^P \left(\frac{\ell^P}{\ell^M}\right)^2 \left(\frac{E^M}{E^P}\right) \left(\frac{\rho^P}{\rho^M}\right) = \ddot{\theta}^P \left(\frac{\ell^P}{\ell^M}\right)^2 \left(\frac{c^M}{c^P}\right)^2
\end{aligned} \tag{45}$$

Here, the one-dimensional (bar) wave speed c appears in the equations and is given by $c = \sqrt{E/\rho}$. In this case, the arbitrary restoring force dimensionless number R_F^N reduces to the Cauchy number, C^N, and the sixth expression in Eq. (43) is trivially satisfied.

Constant Cohesive Strength Restoring Force Density ($S^N := v/\sqrt{\rho/\tau_0}$ Similitude)

In this case, $f_r = \tau_0/\ell$, where τ_0 is a constant cohesive (normal or shear) strength independent of weight, in contrast to the frictional case, and of modulus, in contrast to the elastic case. Here, substitution into Eq. (43) gives

$$
\begin{aligned}
v^M &= v^P \left(\frac{\tau_0^M}{\tau_0^P}\right)^{1/2} \left(\frac{\rho^P}{\rho^M}\right)^{1/2} \\
a^M &= a^P \left(\frac{\ell^P}{\ell^M}\right) \left(\frac{\tau_0^M}{\tau_0^P}\right) \left(\frac{\rho^P}{\rho^M}\right) \\
t^M &= t^P \left(\frac{\ell^M}{\ell^P}\right) \left(\frac{\tau_0^P}{\tau_0^M}\right)^{1/2} \left(\frac{\rho^M}{\rho^P}\right)^{1/2} \\
\dot{\theta}^M &= \dot{\theta}^P \left(\frac{\ell^P}{\ell^M}\right) \left(\frac{\tau_0^M}{\tau_0^P}\right)^{1/2} \left(\frac{\rho^P}{\rho^M}\right)^{1/2} \\
\ddot{\theta}^M &= \ddot{\theta}^P \left(\frac{\ell^P}{\ell^M}\right)^2 \left(\frac{\tau_0^M}{\tau_0^P}\right) \left(\frac{\rho^P}{\rho^M}\right) \\
c^M &= c^P \left(\frac{\tau_0^M}{\tau_0^P}\right)^{1/2} \left(\frac{\rho^P}{\rho^M}\right)^{1/2} \quad \text{or} \\
K^M &= K^P \left(\frac{\ell^M}{\ell^P}\right) \left(\frac{\tau_0^M}{\tau_0^P}\right)
\end{aligned}
\tag{46}
$$

The first five of the above equations depend on the ratio τ_0/ρ in addition to the characteristic length ℓ. The dimensionless number R_F^N reduces to the cohesive strength number $S^N = v\sqrt{\rho/\tau_0}$.

5.3 General Observations and Restrictions on "Scaled" Experimental Design. The sixth equation in each of the groups of Eqs. (43), (44), and (46) represents a scaling requirement imposed by the dimensionless number $\Pi_3 = E/\ell f_r = \rho c^2/\ell f_r$ of Eq. (36) and, as discussed in Sec. 4.4, is a consequence of the inter or intra-block elasticity. This requirement is trivially satisfied in the elastic case (Eq. (45)), so the sixth equation does not appear.

It should again be emphasized that for "similar" rigid block systems, this requirement relating c^M to c^P is not necessary in order to guarantee similitude. In reality, many systems of interest to the field of civil engineering may involve discrete structures made out of concrete or geomaterials that can be considered rigid for most practical purposes. However, there may be other cases when this assumption is violated. Thus, it is important to investigate the constraints to the choices of model material wave speed c^M that such a restriction imposes so that a scaled-down lab experiment can be designed in such a way as to achieve "strict" similitude.

For frictional systems, Eq. (44) applied and provided guidance on how to obtain the ground shaking velocity (or acceleration) time records that need to be applied to a model. Indeed, the first three of these equations show that the velocity or acceleration excitations to be applied to a model of length ℓ^M and friction coefficient μ_s^M should be related to those of a prototype of length ℓ^P and by μ_s^P by

$$
v^M = v^P \sqrt{\lambda_\ell \lambda_\mu}, \quad a^M = a^P \lambda_\mu \tag{47}
$$

where $\lambda_\ell = \ell^M/\ell^P$ and $\lambda_\mu = \mu_s^M/\mu_s^P$, while the time axis of the desired model excitation will have to be scaled to satisfy

$$
t^M = t^P \sqrt{\lambda_\mu/\lambda_\ell} \tag{48}
$$

Here, we have assumed that both model and prototype are located within the same gravitational environment ($g^M = g^P$). This scaling is enough for purely rigid systems. Furthermore, and as we discussed in Sec. 2.3, scaling for such rigid systems remains independent of mass density, and as a result, the density of the chosen model system is not a factor in ensuring similitude. However, when system elasticity becomes important and if $g^M = g^P$, the additional restriction imposed on wave speed similitude (last of Eq. (44)) requires that the blocks of the model structure are made of a material whose one-dimensional wave speed c^M is related to the wave speed c^P of the blocks of the prototype structure by

$$
c^M = c^P \sqrt{\lambda_\mu \lambda_\ell} \tag{49}
$$

While Eqs. (47) and (48) are indeed easy to implement in the lab, Eq. (49) may be difficult to satisfy with common lab materials. As an example, we consider $\lambda_\ell = 0.23$ and $\lambda_\mu = 0.3$, the length and friction coefficient ratios between the experiments described in Sec. 6, respectively. In this example, the prototype material (high-quality concrete) has a 1D (bar) wave speed of $c^P = 4600$ m/s and Eq. (49) predicts a bar wave speed c^M of the model material of $c^M = 1200$ m/s, which is close to the wave speed of "pressed wood" or some soft polymers.

Finally, regarding the choice of frictional parameters in designing model experiments, it should be noted that choosing the friction coefficient of the model to coincide with that of the prototype is not necessary since μ^N scaling also ensures similitude in cases when these coefficients differ. Indeed, the existence of the ratio λ_μ in Eqs. (47)–(49) provides a welcomed flexibility for scaling the excitations of the model to satisfy the desired frequency response and maximum amplitude specifications of laboratory scale shake tables, which often have a variety of performance restrictions.

6 Experimental and Numerical Validation of μ^N Similitude

Our goal here is to explore the issue of consistency across scales. Consistency requires the point-wise similarity between the dynamic motion histories of geometrically similar models and prototypes, provided that the input base excitations are also similar. We will address this issue by using both experimental and numerical comparisons of similar systems involving various block material combinations and friction coefficients, at two different length scales.

Figure 4 displays experiments performed on two multiblock towers, one of which we will call the model (M) of total height $\ell^M = 1.51$ m and made of aluminum (Al) blocks and the other, we will call the prototype (P) of height $\ell^P = 6.46$ m made of concrete blocks. The corresponding block heights were $\ell_0^M = 3.97$ cm and $\ell_0^P = 17$ cm, respectively, giving a ratio of length scales $\lambda_\ell = \ell^M/\ell^P = \ell_0^M/\ell_0^P = 0.23$. The coefficient of friction for the Al blocks was $\mu_s^M = 0.18$ while that of concrete was $\mu_s^P = 0.6$ ($\lambda_\mu = \mu_s^M/\mu_s^P = 0.3$).

The Al tower was tested at the Graduate Aerospace Laboratories at Caltech (GALCIT), while the concrete one at the Pacific Earthquake Engineering Research Center (PEER) at UC Berkeley. Both towers are exact replicas of the 7144 block, real world MTS [28], which has a total height of approximately 25 times that of the concrete tower and 107 times that of the Al tower. The details of tower construction, geometry, choice of base excitation, and measurement diagnostics are discussed in companion publications [29,30]. These papers report on a number of experiments involving MTS of various heights made of wood, Al, and concrete, subjected to a variety of strong, near-fault ground motions corresponding to historical earthquakes of various magnitudes.

In the present work, we will focus on only one Al/concrete tower-pair specifically designed to examine the validity of μ^N similitude. Since the small-capacity shake table used to excite the Al tower at Caltech is only capable of horizontal 1D excitations, this particular concrete tower (tested at the six degrees-of-freedom shaking table at UCB) was also subjected to a 1D motion history. The velocity histories imposed at the base of the model and prototype towers are shown at the bottom of Figs. 4(*c*) and 4(*d*), respectively, and are marked as "base excitations." The two excitation records are related by scaling velocity and time according to Eqs. (47) and (48) which govern the scaling of frictional model/prototype system pairs involving different coefficients of friction in the presence of identical gravitational environments ($g^M = g^P$). Our goal here is to compare experiments conducted on nearly rigid model/prototype systems, intentionally chosen to have very different coefficients of friction, material properties, and masses for the purpose of assessing the limits of the robustness of μ^N similitude.

The color maps in Figs. 4(*a*) and 4(*b*) are representative snapshots of the magnitude of the horizontal component of the particle

velocities parallel to the direction of shaking for the two systems, respectively. These full-field images are obtained through high-speed optical imaging of the tower surface and are enabled by digital image correlation (DIC) [33]. As schematically suggested by Fig. 2(*b*), the temporal sensitivity of optical diagnostics is scaled according to μ^N similitude, while the spatial arrangement is scaled according to system geometry [29,30].

In addition to providing full-field imaging of the overall dynamic deformation behavior of the towers, the optical measurements have enough resolution to provide the time histories of motion of individual blocks within each of the 38 layers (stories) of the towers. These velocity time histories are reported in Figs. 4(*c*) and 4(*d*) for 19 out of the 38 blocks located at the black circles along the height (spine) of each of the towers. We call these time histories the "spine records."

These spine records show the evolution of motion signals propagating up the towers, following the application of similar (μ^N-scaled) excitations at the tower bases. It should be noted that these signals are reported in reference to an "inertial" or "Galilean" frame fixed at a remote location within each laboratory. Most interestingly, these spine records clearly reveal the time scales associated with the propagation of deformation of signals traveling up the two towers. Specifically, they reveal well-defined moments when each layer first senses information arriving from its bottom and is subsequently transmitted to the layer above, block by block. By connecting the points of each of the time histories corresponding to the first measurable deviation of the horizontal velocity history from zero (initial time of signal arrival), one can trace a time/distance line (see Figs. 4(*c*) and 4(*d*)), defining a characteristic speed of transmission in each system. We will call this speed the "structural speed" of the discontinuous system. Another way to measure these structural speeds is through the snapshots of the color maps shown in Figs. 4(*a*) and 4(*b*). These two measurements (from spines or maps) are in excellent agreement and are indeed two sides of the same coin. In each of the two systems shown, the structural speeds are nearly constant (the time/distance line is almost but not perfectly straight). In practice, these speeds were calculated by following a common measurable feature at the initial part of each of the spine records (e.g., Peak A in Fig. 4) as this feature was transmitted from the base to the 37th layer up each of the towers. By using this procedure, the structural speeds at the 37th layer were measured to be 57.5 m/s for the Al tower and 68 m/s for the concrete tower. It should be noted that the elastic wave speeds of Al and concrete are two orders of magnitude larger than these speeds, so this phenomenon is clearly different from the transmission of elastic waves through the structures. Section 7 elucidates the physical meaning of these structural signals by presenting a simple model and comparing it to our experimental observations and numerical calculations discussed in this work.

We now turn to comparing the two systems in order to examine consistency across scales. A first visual inspection of both color maps and spine records reveal an overall signal similarity between the two systems. However, the level of this similarity can only be evaluated in detail if these records (both full-field and spine) are normalized and plotted together in μ^N-space as shown in Fig. 5. In particular, the time axis for both the full-field and the spine records is scaled by dividing time of both model and

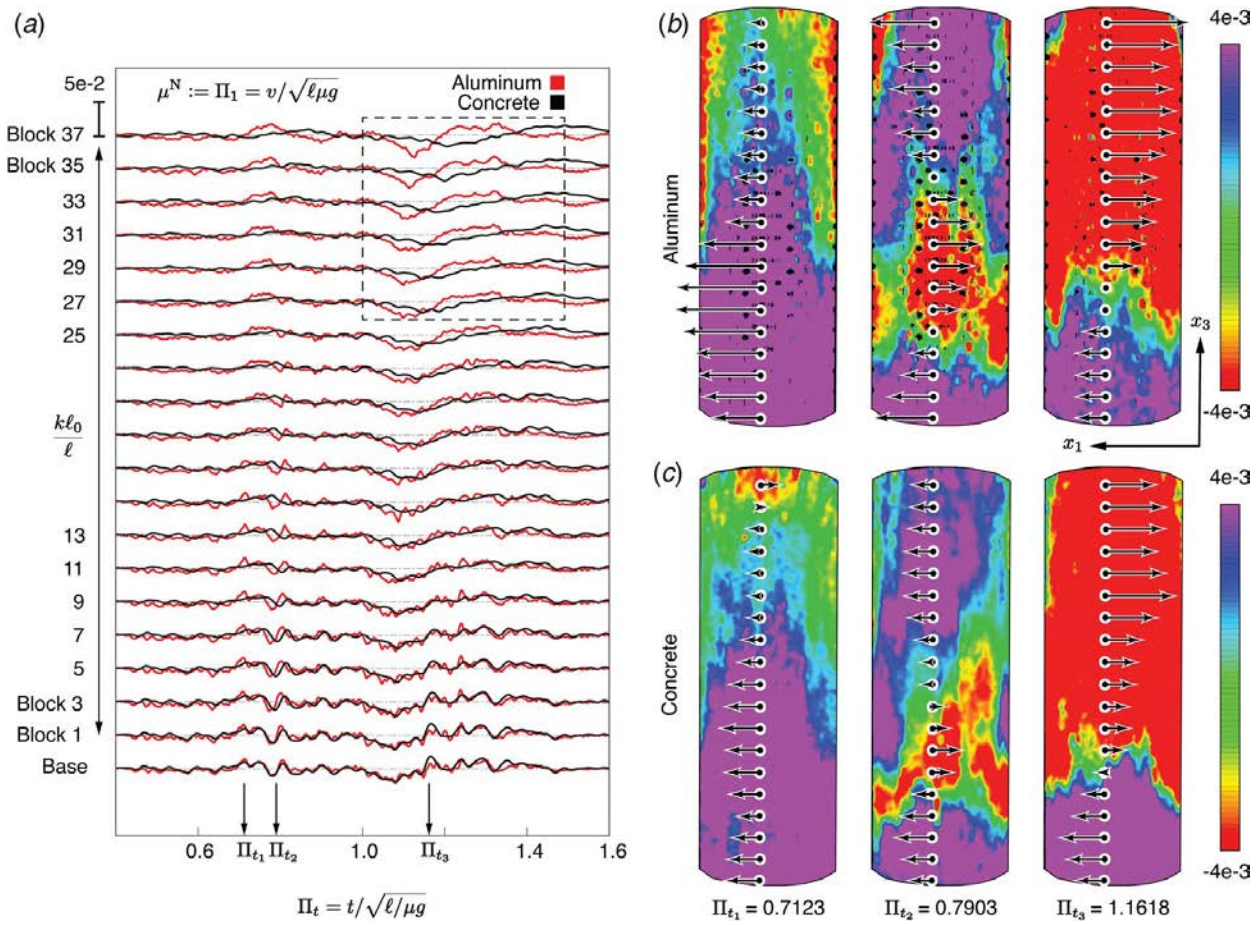

Fig. 5 Comparison of the experimental measurements of Fig. 4 in normalized μ^N-scale. Shown are the dimensionless velocity and time Π groups $\mu^N := \Pi_1 = v/\sqrt{\ell\mu g}$, $\Pi_t = t/\sqrt{\ell/\mu g}$, and dimensionless length corresponding to each of the Al/concrete systems compared for which $\lambda_\ell = \ell^M/\ell^P = 0.23$ and $\lambda_\mu = \mu^M/\mu^P = 0.3$. (*a*) Comparison of the spine time records. (*b*) and (*c*) The normalized velocity fields for Al and concrete, respectively, shown for the same normalized times.

prototype by $\sqrt{\ell/\mu g}$ and particle velocity by $\sqrt{\ell\mu g}$ with ℓ and μ taking the values of ℓ^M, μ_s^M, g^M and ℓ^P, μ_s^P, g^P for the model and prototype, respectively. The vertical axis of these normalized spine plots represents the normalized height $k\ell_0/\ell$ ($k \in [1, n]$) and reduces to 1 at the top of each system.

We first start by comparing the color and vector plots corresponding to the two systems, now normalized as described earlier (see Fig. 5). The structure of these snapshots corresponding to the same normalized times looks very similar, providing confidence in the robustness of the scaling (multiscale consistency). Discrete data from these normalized plots can now be used to produce a normalized spine record. This record is shown in Fig. 5(*a*). Figure 5(*a*) reveals the collapse of the experimental measurements along the spine into a single spine record in μ^N-space. Within experimental error, the two time histories are literally on top of each other for the first 25 out of the 38 levels of the tower. However, small differences begin to develop at higher levels and at longer times, as highlighted by the dashed rectangle. Despite these differences, it is still quite remarkable that the dynamic response of two towers of very different heights (one at lab scale and the other almost two stories tall) and featuring very different block materials and friction coefficients can be shown to scale properly when μ^N scaling is applied.

One reason for the observed differences is likely due to the inability of the shake table at UC Berkeley to reproduce in detail the desired, scaled base excitation record of the much smaller Caltech table with high-fidelity. These two base excitation records, shown at the bottom of the normalized spine plot of Fig. 5(*a*), need to coincide in order to impose similitude at the base. Another reason may be related to the importance of elasticity of each system. As discussed in Sec. 5.3, if the materials in the model/prototype pair are sufficiently elastic, in addition to Eqs. (47) and (48), μ^N scaling requires that Eq. (49) should also be satisfied for complete similitude to be achieved (i.e., for all dimensionless numbers to be equal between model and prototype). Indeed, for $\lambda_\ell = \ell^M/\ell^P = 0.23$, $\lambda_\mu = \mu^M/\mu^P = 0.3$ and for the Al ($c^M = 6,\ 400$ m/s)/concrete ($c^P = 4,\ 600$ m/s) pair, this equation is clearly violated.

In order to eliminate the experimental uncertainties and to also investigate the necessity of satisfying Eq. (49) in achieving perfect μ^N similitude, we now resort to detailed numerical simulations of our tower systems. These dynamic simulations, which make use of the well established LS-DEM methodology, have themselves been extensively validated [28,31] and can be used as a proxy to the elaborate and expensive shake table experiments.

We start by using LS-DEM to first investigate similitude in the same Al/concrete system pair used in the experiments shown in Figs. 4 and 5. Here, the base excitations of the Al tower can be perfectly scaled to excite the larger scale concrete tower, avoiding experimental inconsistencies in base excitations. Figure 6(*a*) shows the spine records corresponding to the two calculations again plotted together in the same normalized μ^N-space used to present the experimental results in Fig. 5. Again, the agreement between the Al (red) and concrete (black) time records remains remarkable until the 27th level and in the remaining levels exhibits some differences (highlighted by the dashed rectangle), similar to those observed in its experimental counterpart. The similarity between the normalized spine records obtained experimentally (Fig. 5(*a*)) and numerically (Fig. 6(*a*)) demonstrates that the experimental difficulties of producing perfectly scaled base excitation records between models and prototypes are not the reason for the observed differences outlined in the rectangles.

To further investigate this issue, we now consider a new set of calculations involving a purely hypothetical model/prototype pair for which Eq. (49) is satisfied. For this case, the bar wave speed

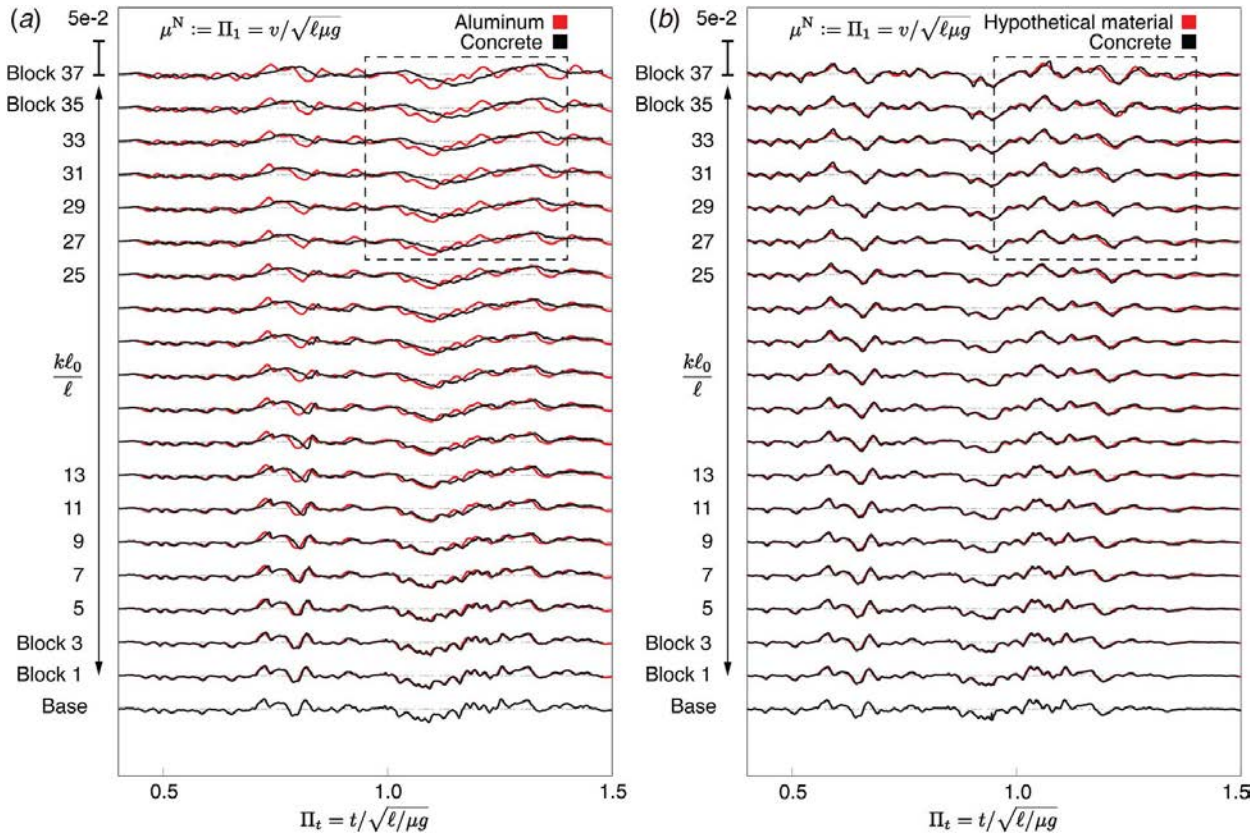

Fig. 6 Comparison of the results of LS-DEM simulations in normalized μ^N-space. (*a*) An Al/concrete model/prototype pair ($\mu^M = 0.18$, $\mu^P = 0.6$, $\lambda_\mu = 0.3$, $\lambda_\ell = 0.23$) same as in the experimental comparison presented in Fig. 5. (*b*) A hypothetical material/concrete model/prototype pair ($\mu^M = 0.18$, $\mu^P = 0.6$, $\lambda_\mu = 0.3$, $\lambda_\ell = 0.23$) for which also $c^M = c^P\sqrt{\lambda_\mu\lambda_\ell}$ ($c^M \sim 1,\ 200$ m/s, $c^P \sim 4,\ 600$ m/s), satisfying the dimensionless requirement arriving from block elasticity.

of the hypothetical model material is $c^M \sim 1200$ m/s, while the prototype is $c^P \sim 4600$ m/s (concrete) with $\lambda_\ell = 0.23$ as before. Moreover, the coefficient of friction of this hypothetical material is kept at $\mu_s^M = 0.18$ (as in Al) and that of concrete $\mu_s^M = 0.6$ as before. The above choices of wave speeds (moduli and mass densities) affect the inter-block elasticity in the LS-DEM calculation whose inter-block elastic spring constants are now in accordance to the last of Eq. (44). The results of this calculation are again displayed in μ^N-space and are shown in Fig. 6(*b*). This figure shows that the spines for the model and the prototype are now virtually indistinguishable at all the tower levels. This remarkable collapse of the records into a single normalized spine in μ^N-space is consistent with the theoretical requirement that in the presence of elasticity, the last dimensionless group in Eqs. (41) and (42) (leading to Eq. (49)) also needs to be satisfied for complete similitude. In other words, it demonstrates the ability of μ^N scaling for frictional systems in the presence of elasticity to deliver complete multiscale consistency.

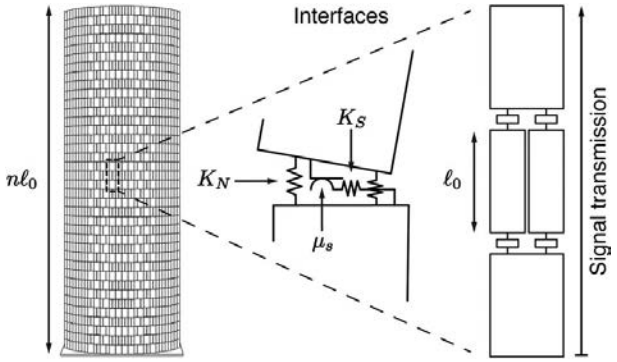

Fig. 7 The combination of elastic springs (normal and horizontal) and frictional element (horizontal) providing restoring forces between rigid blocks, as assumed in formulating the model for structural signal transmission. This model is consistent with LS-DEM methodology.

7 The Concept of Structural Speed in Frictional Discontinuous Structures

When multiblock frictional structures of the type motivating this study are subjected to seismic excitation at their bases, structural deformation signals of block acceleration, velocity, or displacement histories are observed to propagate up the structure with very well defined and experimentally measurable speeds. These speeds are typically a couple of orders of magnitude slower than the elastic wave speeds of the individual block material.

For very "stiff" multiblock systems in which each of the constituent blocks can be considered as being rigid, these signals are the only available mechanism to transmit information along the structure given the fact that, within the rigid approximation, the individual block wave speeds are infinite. Examples of this behavior were discussed in Sec. 6.

In this section, we describe a simple model whose goal is to investigate the system parameters which govern the speed of signal transmission in discrete, frictional structures subjected to primarily horizontal excitations and to reveal the dependence of this speed on system variables.

7.1 A Simple Model for Structural Signal Transmission.

We consider n layers of blocks stacked on top of each other as shown in Fig. 7. The nominal height of each layer coincides with the nominal height of each block and is equal to ℓ_0. The first layer of blocks sits on a base of the same material and surface properties as each of the individual blocks. Any relative motion of the kth interface, located at the bottom of the kth layer, is resisted by shear and normal resisting forces operating at each of the inter-block and block-base interfaces. The normal forces arising due to contact are compressive and only resist block interpenetration, with no resistance offered to interfacial opening between blocks and layers. The shear and normal forces averaged over the length of each interface will be denoted by F_S^k and F_N^k, respectively. They represent the "effective" resistance offered by the bottom of each layer k ($1 \le k \le n$) to sliding or interpenetration in the presence of multiple contact points being generated along each of the interfaces during the motion history of the multi-layer structure. The total number of interfaces is equal to the total number of layers and is thus equal to n, while the total height of the multi-layer structure is equal to $\ell = n\ell_0$.

For structures composed of blocks that are rigid, or nearly rigid, the interface between blocks and layers is the only mechanism of transmitting deformation signals across the structure. The collective action of the interfaces determines the time needed for signals from the base to travel up the height of the tower and defines the "structural speed" of the system. The effective time that a signal from the base takes to be transmitted to the top of the first block will be denoted here as ΔT^1. Similarly, ΔT^k will be the time that a signal takes to travel from the top of block $k-1$ to the top of block k. Since these blocks are rigid, the times ΔT^k are only characteristic of each interface (both elastic and frictional) and may also depend on the details of individual block contacts (e.g., number of active contact points) at each level. Given the above, the total time T^k for information generated by the base excitation to reach the top of the kth layer of blocks can now be expressed by

$$T^k = \sum_{i=1}^{k} \Delta T^i \tag{50}$$

where $1 \le k \le n$. This time is also equal to the total height of the first k layers, $k\ell_0$, divided by the average speed, V^k, of a structural signal arrival at the top of the kth level (i.e., $T^k = (k\ell_0)/V^k$). By definition and by using Eq. (50), we can now write

$$V^k := \left[\frac{1}{\frac{1}{k}\sum_{i=1}^{k} \Delta T^i} \right] \ell_0 \tag{51}$$

The average speed V^k will be called the "structural speed" of a signal generated at the base and arriving at the top of level k. This speed is not necessarily constant and will in general be a function of height or, equivalently, it may be thought of as a discrete function of k. Equation (51) shows that V^k depends on the arithmetic mean of the times ΔT^i needed for each interface i ($1 \le i \le k$) to transmit a signal to the rigid block i situated just above it. Since the structural speed V^k at layer k is a speed that can be measured (see Figs. 4(*a*) and 4(*b*)), it is useful to relate it to basic elastic and frictional interfacial contact properties of force transmission at each of the k layers with the goal of providing scaling relations between "similar" model/prototype systems. To achieve this, we look at each of the k layer interfaces and adopt the physical description employed by the popular LS-DEM model [31,32] which has been successful in describing the mechanism of force transmission between rigid blocks or grains in frictional contact. With this methodology in mind, the time ΔT^k can be identified with t_f^k, where t_f^k is the time needed to commence frictional sliding at the kth interface (i.e., $\Delta T^k = t_f^k$).

Within the LS-DEM framework, single normal contacts are first resisted by the compression of elastic springs of normal stiffness K_N, while sliding is first resisted by elastic springs of shear stiffness K_S until a threshold corresponding to a constant friction coefficient is reached. In our simple model, these stiffnesses will represent the average stiffness of each block-to-block interface and will be considered the same at all interfaces.

Within the present idealization, t_f^k is the time when the average value of sliding at the bottom of the kth layer becomes large enough for the average shear resisting force F_S^k to reach $\mu_s^k F_N^k$, where μ_s^k is the friction coefficient of the kth interface, thus entering the sliding regime at the bottom of layer k. This time defines the instant beyond which substantial sliding may occur at constant friction coefficient μ_s^k.

To estimate t_f^k, we recall that within the elastic regime $dF_S^k = K_S v_S^k dt$, where dF_S^k is the increment of the shear resistance, v_S^k is the relative average sliding speed between the bottom of layer k and the top of layer $k-1$, and dt is the time increment. Integration of this expression from $t=0$ to $t=t_f^k$, at which time $F_S^k = \mu_s^k F_N^k$, gives:

$$F_S^k(t_f^k) = \int_{F_S^k=0}^{F_S^k=\mu_s^k F_N^k} dF_S^k = \mu_s^k F_N^k(t_f^k) = K_S \int_0^{t_f^k} v_S^k(t)\, dt \tag{52}$$

If we now define $\dot{\delta}_S^k$ as the time-averaged relative sliding speed between the kth and the $k-1$ layers as

$$\dot{\delta}_S^k := \frac{1}{t_f^k} \int_0^{t_f^k} v_S^k(t)\, dt \tag{53}$$

then Eqs. (52) and (53) yield

$$F_S^k(t_f^k) = \mu_s^k F_N^k(t_f^k) = K_S \dot{\delta}_S^k t_f^k \tag{54}$$

We further know that according to the LS-DEM model, the normal force F_N^k at time t_f^k can be expressed as [28,31]:

$$F_N^k = (K_N d^k - c^k \dot{\delta}_N^k) \tag{55}$$

where d^k and $\dot{\delta}_N^k$ are averages (over the kth interface) of the interpenetration distance and the relative normal velocity between blocks, respectively, while c^k is the average of the coefficient of restitution at the kth level. Equations (54) and (55) now yield:

$$\mu_s^k (K_N d^k - c^k \dot{\delta}_N^k) = K_S \dot{\delta}_S^k t_f^k \tag{56}$$

By assuming that $K_N d^k \gg c^k \dot{\delta}_N^k$, an assumption which is strictly true for shear-dominated motions between blocks (i.e., $\dot{\delta}_N^k = 0$) or for inelastic collisions of blocks (i.e., $c^k = 0$), and by recalling that $\Delta T^k = t_f^k$, Eq. (56) can be solved for ΔT^k to yield:

$$\Delta T^k = \left(\frac{K_N}{K_S}\right) \frac{d^k \mu_s^k}{\dot{\delta}_S^k} \tag{57}$$

By substituting Eq. (57) into Eq. (51), the structural speed V^k can now be expressed as follows:

$$V^k = \frac{k\ell_0}{\sum_{i=1}^k \left(\frac{K_N}{K_S}\right) \frac{d^i \mu_s^i}{\dot{\delta}_i^k}} \tag{58}$$

where V^k is the speed of a structural signal arriving at the top of the kth layer for every $k \in [1, n]$.

7.2 Consequences of Imposing Similitude to the Functional Form and Scaling of Structural Speeds: The Case of Uniform Coefficient of Friction. After establishing a general expression for the structural speed V^k, our goal now becomes to use the scaling relations derived in Secs. 4.3 and 5.2 for systems of blocks featuring frictional restoring forces in the presence of some system elasticity to also investigate the dependence of ΔT^k and V^k on geometry and to thus derive scaling laws governing the interrelation of the structural speeds of "similar" model/prototype systems. In this section, we first assume that the coefficient of friction for each interface is the same (i.e., $\mu_s^k = \mu_s$) but will in general be different between a model and a prototype system (i.e., $\mu_s^M \neq \mu_s^P$). We will then generalize this result to friction coefficients which vary from interface to interface.

To scale the structural speeds, we first recall that the system dynamics in these cases are described in a dimensionless form by Eq. (41) with $\mu = \mu_s$ (for a frictional system) as

$$\tilde{g}(\Pi_1; \Pi_2; \Pi_3) = \tilde{g}\left(\frac{v}{\sqrt{\ell \mu_s g}}; \frac{a}{\mu_s g}; \frac{K}{\ell^2 \mu_s \rho g}\right) = 0 \tag{59}$$

where the dimensionless numbers Π_1, Π_2, and Π_3 will govern the scaling according to μ^N similitude.

The first dimensionless number Π_1 in Eq. (59) requires that for a system of total height $\ell = n\ell_0$ all particle speeds, and as a consequence, the relative sliding speed $\dot{\delta}_S^k$ at each level will be proportional to $\sqrt{\ell \mu_s g}$ and will have the form:

$$\dot{\delta}_S^k = \sqrt{\ell \mu_s g}\ \Pi_1^k(\Pi_2; \Pi_3) \tag{60}$$

In Eq. (60), Π_1^k is a position-dependent (through k) function of the second- and third-dimensionless groups Π_2 and Π_3, a fact which reflects the scaling of the base motions to achieve similitude between a model and prototype system, i.e., $(v/\sqrt{\ell \mu_s g})^M = (v/\sqrt{\ell \mu_s g})^P$. The dependence of Π_1^k on k merely recognizes the possibility of variations of average sliding speed from layer to layer.

Furthermore, similitude as described by Eq. (59) also requires that each of the elastic stiffnesses K_N and K_S scale as $\ell^2 \mu_s \rho g \Pi_3$, while their ratio K_N/K_S will be a constant dimensionless number R which will remain the same for a model/prototype system. This ratio is typically chosen to be of the order of unity in LS-DEM calculations of rigid block or particle systems [31].

Finally, the vertical interpenetration distance d^k is expected to simply scale with the characteristic block length ℓ_0 and to also vary from layer to layer as follows:

$$d^k = \ell_0\ \Pi_0^k(\Pi_1; \Pi_2; \Pi_3) \tag{61}$$

where Π_0^k is a dimensionless function of the three dimensionless variables of the system.

By substituting Eqs. (60) and (61) into Eq. (57), the average time ΔT^k for transmitting a frictional signal across the kth layer becomes

$$\Delta T^k = \ell_0 \left(\frac{\mu_s}{\ell g}\right)^{1/2} \Pi^k \tag{62}$$

where $\ell = n\ell_0$ and $\Pi^k(\Pi_1; \Pi_2; \Pi_3) := R\Pi_0^k/\Pi_1^k$ is an unknown function of Π_1, Π_2, and Π_3.

Further substitution of Eqs. (60) and (61) into Eq. (58) gives the expression for the structural speed at level k as

$$V^k = \left(\frac{\ell g}{\mu_s}\right)^{1/2} \left[\frac{k}{\sum_{i=1}^k \Pi^i}\right] \tag{63}$$

The quantity in brackets in the above equation is a function of level k, and as such it represents the height variation of V^k as this is influenced by the additive contributions of each of the preceding layers. Its denominator is a function of the dimensionless groups Π_1, Π_2, and Π_3 only.

We will now consider a model (M) and prototype (P) system such that the base excitations observe $(v/\sqrt{\ell \mu_s g})^M = (v/\sqrt{\ell \mu_s g})^P$ and $(a/\mu_s g)^M = (a/\mu_s g)^P$, and also $(K/\ell^2 \mu_s \rho g)^M = (K/\ell^2 \mu_s \rho g)^P$. For such systems $\Pi_1^M = \Pi_1^P$, $\Pi_2^M = \Pi_2^P$, and $\Pi_3^M = \Pi_3^P$, ensuring full μ^N similitude at each level k as long as the two systems are geometrically similar, i.e., they have the same number of interfaces $n^M = n^P$.

As a result, we have

$$\left[\frac{k}{\sum_{i=1}^{k}\Pi^i}\right]^M=\left[\frac{k}{\sum_{i=1}^{k}\Pi^i}\right]^P \tag{64}$$

since for each corresponding layer, $k^M=k^P$, and $[\Pi^k]^M=[\Pi^k]^P$ which is true, since Π^k is only a function of Π_1, Π_2, and Π_3 and these three must be invariant for the systems to remain "similar."

By applying Eq. (63) to both systems, dividing by sides, invoking Eq. (64) and recalling that $\ell=n\ell_0$ and that $n^M=n^P$, one gets a scaling relation between the structural speeds $(V^k)^M$ and $(V^k)^P$ as follows:

$$(V^k)^P=(V^k)^M\left(\frac{\ell_0^P}{\ell_0^M}\right)^{1/2}\left(\frac{g^P}{g^M}\right)^{1/2}\left(\frac{\mu_s^M}{\mu_s^P}\right)^{1/2} \tag{65}$$

$\forall k\in[1,n]$. Equation (65) holds for each of the individual layers k between model and prototype and does not assume that the structural speed is constant at each level. However, it strictly holds when comparing "similar" model/prototype systems such that their base excitations have been scaled to assure μ^N similitude. Finally, it should be noted that in the above relation the ratio ℓ_0^P/ℓ_0^M is also equal to ℓ^P/ℓ^M (ratio of total heights) since for Eq. (65) to strictly hold, the two structures also need to be geometrically similar, i.e., $n^M=n^P$.

7.3 Generalization to Different Coefficients of Friction At Each Level. Here, we will generalize the results obtained in Sec. 7.2 to include arbitrary variations of friction coefficient from layer to layer, as long as these variations are kept "similar" between a model and a prototype. To do so, we express the coefficient of friction μ_s^k at the bottom interface of the kth layer as $\mu_s^k=\mu_0\hat{\mu}(k)$, where μ_0 is a common amplitude, say its value at the bottom layer of the structure, while $\hat{\mu}(k)$ represents its discrete height variation with k, from $k=1$ to $k=n$. Note that the discussion of structural speed presented in Sec. 7.1 and in particular Eqs. (57) and (58) have already been derived by considering different coefficients of friction μ_s^k at each layer. In this general case and if the height variations of the frictional coefficients $\hat{\mu}(k)$ are purposefully kept the same, i.e., $\hat{\mu}(k)^P=\hat{\mu}(k)^M$, the sliding speed at the kth interface will have the form:

$$\dot{\delta}_S^k=\sqrt{\ell\mu_0 g}\;\Pi_1^k(\Pi_1;\Pi_2;\Pi_3) \tag{66}$$

provided that the excitations at the bases are related by $(v/\sqrt{\ell\mu_s g})^M=(v/\sqrt{\ell\mu_s g})^P$, $(a/\mu_s g)^M=(a/\mu_s g)^P$ and $(K/\mu_s\rho g\ell^2)^M=(K/\mu_s\rho g\ell^2)^P$, while $\hat{\mu}(k)^M=\hat{\mu}(k)^P$, i.e., Π_1 and Π_2 are evaluated for $\mu=\mu_0$.

Here, the interpenetration distance of Eq. (61) becomes:

$$d^k=\ell_0\;\Pi_0^k(\Pi_1;\Pi_2;\Pi_3) \tag{67}$$

By substituting Eqs. (66) and (67) into Eq. (57), we get

$$\Delta T^k=\ell_0\left(\frac{\mu_0}{(n\ell_0)g}\right)^{1/2}\sqrt{\hat{\mu}(k)}\;\Pi^k \tag{68}$$

where $\Pi^k(\Pi_1;\Pi_2;\Pi_3):=R\Pi_0^k/\Pi_1^k$ and R is the constant ratio of stiffnesses K_N/K_S as described in Sec. 7.2. Further substitution of Eq. (68) into Eq. (58) yields

$$V^k=\left(\frac{n\ell_0 g}{\mu_0}\right)^{1/2}\left[\frac{k}{\sum_{i=1}^{k}\sqrt{\hat{\mu}(i)}\;\Pi^i}\right] \tag{69}$$

where the quantity in square brackets represents the discrete variation of V^k along the height.

If similitude is assured between model/prototype systems, here again, the quantity in brackets remains invariant between the model and the prototype, and as a result,

$$(V^k)^P=(V^k)^M\left(\frac{\ell_0^P}{\ell_0^M}\right)^{1/2}\left(\frac{g^P}{g^M}\right)^{1/2}\left(\frac{\mu_0^M}{\mu_0^P}\right)^{1/2} \tag{70}$$

which is the equation relating the structural speeds $(V^k)^M$ and $(V^k)^P$ for each level $k\in[1,n]$. Equations (69) and (70) are the generalizations of Eqs. (63) and (65) for arbitrarily varying coefficients of friction $\mu_s^k=\mu_0\hat{\mu}(k)$ along the height of the structure and reduce to their constant coefficient equivalent when $\hat{\mu}(k)=1$ and $\mu_s^k=\mu_0=\mu_s$.

7.4 The Special Case of Constant Structural Speed. Here, we briefly examine the particular case of systems of identical friction coefficients between layers ($\mu_s^k=\mu_s$) in which the structural speed is measured to be constant. In such systems, the structural signal reaches each level with the same average speed V such that

$$V^k=V,\quad\forall\;k\in[1,n] \tag{71}$$

Applying the above experimentally supported hypothesis for $k=1$ and $k=2$ requires that $V^1=V^2$ and Eq. (63) gives

$$\frac{1}{\Pi^1}=\frac{2}{\Pi^1+\Pi^2} \tag{72}$$

which can only hold if $\Pi^1=\Pi^2$. However, since Eq. (71) holds for all $k\in[1,n]$, its sequential application implies that

$$\Pi^k=\Pi \tag{73}$$

where Π is independent of level k in the structure but is undetermined by this analysis.

By substituting Eq. (73) into Eq. (63), we obtain the value of this constant structural speed as

$$V^k=V=\left(\frac{\ell g}{\mu_s}\right)^{1/2}\frac{1}{\Pi} \tag{74}$$

where Π still remains an unknown function of the dimensionless groups Π_1, Π_2, and Π_3. Furthermore, in this special case, the structural speed arriving at each level k is constant, and as such, it is insensitive to the number of previous interfaces lying below level k in the stack. One would also expect that Π is itself insensitive to the above discussed dimensionless groups and to be just a real number. Indeed, this expectation is rationalized by considering the subset of the structure composed of only layers above level k. This subset experiences excitations which are different than those of the base; yet, its structural speed remains the same as in the layer below and is also independent of the exact nature of the base excitation. If this insensitivity is true, one could compare model/prototype systems of various total heights ℓ and in which strict similitude is not imposed at their base since Π is not sensitive to the value of the three invariants Π_1, Π_2, and Π_3. Furthermore, since V is insensitive to the total number of interfaces n, one can even provide scaling relations for V between model/prototype systems featuring different numbers of interfaces, i.e., $n^M\neq n^P$, rather than on their total heights.

The scaling laws for such systems can now be obtained by Eq. (74) as

$$(V)^P=(V)^M\left(\frac{\ell^P}{\ell^M}\right)^{1/2}\left(\frac{g^P}{g^M}\right)^{1/2}\left(\frac{\mu_s^M}{\mu_s^P}\right)^{1/2} \tag{75}$$

which is a relation very similar to Eq. (65) or (70) but with ℓ_0 replaced by the total height ℓ without requiring that $n^P=n^M$.

7.5 Discussion and Experimental Validation. We first observe that the scaling Eqs. (65) and (70) providing the ratio V^P/V^M of the structural speeds (constant or not) of a model to a prototype in various cases are very similar in structure. They also share the interesting property that they only involve ratios of lengths

and friction coefficients (for the same gravitational environment) without any dependence on elastic material properties such as K_N, K_S, or mass density. In general, this property only holds for the ratios V^P/V^M and may not be true for each of the structural speeds (see Eq. (63) or (69)) which may also depend on density and elasticity through the dimensionless groups $\Pi_3 = K/\mu_s \rho g \ell^2$ or $c^2/\ell\mu_s\, g$. The particular special case of constant structural speed is however noteworthy, since both the ratio and the actual values of V may only depend on ℓ, g, and μ_s with no sensitivity on density or elasticity as discussed in Sec. 7.4.

In order to experimentally validate the above scaling relations, we refer to the spine records of Fig. 4 for the Al/concrete model/prototype system pair described in Sec. 6. For this particular model/prototype pair, $\ell^M/\ell^P = 0.23$, $g^M/g^P = 1$, $\mu_s^M/\mu_s^P = 0.3$, and the structural speed near the top of the Al tower ($k = 37$) was measured to be $(V^{37})^M = 57.5$ m/s. By substituting the above values into Eq. (65), which does not assume that the structural speed is constant, we predict that the structural speed of the concrete tower at the equivalent block level should be equal to $(V^{37})^P \sim 65.6$ m/s. This theoretical prediction is very close to the measured structural speed of 67.9 m/s recorded at the top of the concrete tower.

Additional measurements of structural speeds can also be used to demonstrate the predictive nature of scaling Eq. (65). Such measurements are reported in Refs. [29,30]. In particular, measurements of structural speeds on wooden towers reported in these references allow us to compare with the speeds reported for the Al system described in Sec. 6. These wooden towers are geometrically identical to the Al towers, but feature a friction coefficient of 0.63. By considering the Al/wood system as the model/prototype system pair, with $\lambda_\ell = 1$, $\lambda_\mu = \mu_s^M/\mu_s^P = 0.18/0.63 = 0.29$ and by using the measured value $(V^{37})^M = 57.5$ m/s for Al, Eq. (65) now predicts $(V^{37})^P = 31.5$ m/s for the wooden prototype. This prediction is very close to the value of 33.5 m/s directly measured in Ref. [29] by means of both full-field DIC and point-wise laser velocimeter records.

The accuracy of these predictions involving geometrically similar systems at different scales and/or coefficients of friction provides confidence on the validity of the scaling equations and the ability of our simple model to capture the physics of structural signal transmission in discrete multiblock systems across scales (consistency).

8 Concluding Remarks

Unlike continuous systems that are prevalent in the modern build environment, very little is known regarding the identification of dimensionless numbers capable of accurately capturing the physical mechanisms governing the dynamic deformation and scaling in discontinuous MTS. Indeed, the presence of numerous interfaces in such systems governs the overall dynamic response, and as a result, particular attention must be paid to physics which determine the interface behavior.

The current work introduces and validates a general theoretical framework describing the behavior of MTS when subject to inertial loading and introduces a dimensionless "Arbitrary Restoring Force Number" (R_F^N) with its associate scaling laws. This general framework allows us to consistently explore the effect of different types of interfaces on similitude, revealing their similarities and differences. Examples of interface types include but are not limited to frictional, gravitational, cohesive, viscous, elastic, and mixed restoring forces. In addition to interfacial mechanics, the analysis also allows us to explore the consequences of intra-block elasticity, thus accounting for block deformability.

Not surprisingly, the analysis shows that in most cases and with only a few notable exceptions, classical Cauchy and Froude number similitudes currently employed in seismic testing of structures fail to provide appropriate scaling laws since they do not accurately reflect the detailed physical restoring force generation and dissipation at the interfaces. This result has immediate practical consequences on the design of small-scale model experiments whose purpose is to study the full-scale seismic performance of system prototypes. Here, our analysis provides specific guidelines on material selection and laws to be employed for scaling the applied seismic excitation for each type of interface. Equivalently, our methodology guides the appropriate choices of both interfacial and bulk material properties of numerical models (e.g., discrete element models) ensuring their predictive ability when applied to various length and time scales.

Particular attention is paid to the special case of discontinuous structures featuring "frictional" interfaces, motivated by MTS currently proposed for renewable energy storage applications (potential energy batteries). To evaluate the resilience of such frictional systems to seismic excitations, we introduce the frictional/gravitational dimensionless "mu-Number" (μ^N) and explore the concept of μ^N similitude. This concept is used to design a series of appropriately scaled model experiments at two different length scales, allowing us to validate and to demonstrate the usefulness of μ^N similitude in describing the dynamics of frictional discontinuous structures of various material properties and scales, ensuring multiscale consistency.

Finally, motivated by multiscale experimental observations, we introduce the concept of "structural speed" and present a simple model explaining the mechanics of structural signal transmission in frictional multiblock systems.

The results presented in this study are only a part of a wider campaign undertaken by our group. They describe the theoretical development and validation of basic tools and concepts necessary for carrying out a coordinated theoretical, experimental, and numerical campaign designed to explore the seismic resilience of various types of discontinuous Multiblock Tower Structures.

Acknowledgment

This research was supported by Energy Vault, Inc. We gratefully acknowledge Energy Vault's support, encouragement and freedom during this project. We also thank the contractors (Whiteside Concrete Construction, Dynamic Isolation Systems, BlockMex, TCI Precision Metals, AbelCine, Samy's Camera, Luka Grip & Lighting, DTC Lighting & Grip), and university facility personnel at UCB and Caltech for their commitment to this project.

Data Availability Statement

The authors attest that all data for this study are included in the paper.

References

[1] Buckingham, E., 1914, "On Physically Similar Systems; Illustrations of the Use of Dimensional Equations," Phys. Rev., **4**(4), pp. 345–376.
[2] Rayleigh, L., 1915, "The Principal of Similitude," Nature, **95**(2368), pp. 66–68.
[3] von Kármán, T., and Lin, C. C., 1949, "On the Concept of Similiarity in the Theory of Isotropic Turbulence," Rev. Mod. Phys., **21**(3), pp. 516–519.
[4] Barenblatt, G. I., 1996, *Scaling, Self-Similarity, and Intermediate Asymptotics* (Cambridge Texts in Applied Mathematics), Cambridge University Press, Cambridge.
[5] Bažant, Z. P., and Kazemi, M. T., 1990, "Determination of Fracture Energy, Process Zone Length and Brittleness Number From Size Effect, With Application to Rock and Concrete," Int. J. Fracture, **44**(2), pp. 111–131.
[6] Bažant, Z. P., 1976, Instability, "Ductility, and Size Effect in Strain-Softening Concrete," J. Eng. Mech. Div., **102**(2), pp. 331–344.
[7] Harris, G. H., and Sabnis, M., 1999, *Structural Modeling and Experimental Techniques*, 2nd ed., CRC Press, Boca Raton.
[8] Moncarz, P. D., and Krawinkler, H., 1981, "Theory and Application of Experimental Model Analysis in Earthquake Engineering, The John A. Blume Earthquake Engineering Center," Department of Civil Engineering, Stanford University, SAE Technical Paper 50.
[9] Thune, N. A., 2005, Kheops Pyramid, Cairo, Egypt, https://upload.wikimedia.org/wikipedia/commons/e/e3/Kheops-Pyramid.jpg
[10] Storeye, 2007, The Temple of Hephaistos in Athens, Athens, Greece, https://upload.wikimedia.org/wikipedia/commons/0/0c/Hephaistos_Temple.JPG
[11] Lu, J., Zhang, Y., and Yao, Q., 2008, "Analysis of Seismic Disaster of Masonry Pagodas," *Geotechnical Engineering for Disaster Mitigation and Rehabilitation*, Liu, H., Deng, A., and Chu, J., Springer Berlin Heidelberg, Berlin, Heidelberg, pp. 381–386.

[12] Tong, D. Y., 2012, Burj Khalifa, Dubai, United Arab Emirates, https://upload.wikimedia.org/wikipedia/en/9/93/Burj_Khalifa.jpg
[13] Housner, G. W., 1963, "The Behavior of Inverted Pendulum Structures During Earthquakes," Seismol. Soc. Am., **53**(2), pp. 403–417.
[14] Spanos, P. D., and Koh, A., 1984, "Rocking of Rigid Blocks Due to Harmonic Shaking," J. Eng. Mech., **110**(11), pp. 1627–1642.
[15] Shenton III, H. W., and Jones, N. P., 1991, "Base Excitation of Rigid Bodies. I: Formulation," J. Eng. Mech., **117**(10), pp. 2286–2306.
[16] Shenton III, H. W., and Jones, N. P., 1991, "Base Excitation of Rigid Bodies. II: Periodic Slide-Rock Response," J. Eng. Mech., **117**(10), pp. 2307–2328.
[17] Ulm, F., and Piau, J. M., 1993, "Fall of a Temple: Theory of Contact Applied to Masonry Joints," J. Struct. Eng., **119**(3), pp. 687–697.
[18] Shenton III, H. W., 1996, "Criteria for Initiation of Slide, Rock, and Slide-Rock Rigid-Body Modes," J. Eng. Mech., **122**(7), pp. 690–693.
[19] Dimitrakopoulos, E. G., and DeJong, M. J., 2012, "Revisiting the Rocking Block: Closed-Form Solutions and Similarity Laws," Proc. R. Soc. A, **468**(2144), pp. 2294–2318.
[20] Makris, N., 2014, "A Half-Century of Rocking Isolation," Earthq. Struct., **7**(6), pp. 1187–1221.
[21] Kounadis, A. N., 2018, "The Effect of Sliding on the Rocking Instability of Multi-Rigid Block Assemblies Under Ground Motion," Soil Dyn. Earthq. Eng., **104**, pp. 1–14.
[22] Kounadis, A. N., 2019, "Seismic Instability of Free-Standing Statues Atop Multispondyle Columns: A Heuristic Very Stable System of Ancient Technology," Soil Dyn. Earthq. Eng., **119**, pp. 253–264.
[23] Konstantinidis, D., and Makris, N., 2005, "Seismic Response Analysis of Multidrum Classical Columns," Earthq. Eng. Struct. Dyn., **34**(10), pp. 1243–1270.
[24] Korres, M., 1996, "Seismic Damage to the Monuments of the Athenian Acropolis," *Archaeoseismology*, S. Stiros and R. Jones, eds., Fitch Laboratory Occasional Paper 7, Institute of Geology & Mineral Exploration & The British School at Athens, Athens, Greece, pp. 69–74.
[25] Stiros, S. C., 2020, "Monumental Articulated Ancient Greek and Roman Columns and Temples and Earthquakes: Archaeological, Historical, and Engineering Approaches," J. Seismol., **24**(4), pp. 853–881.
[26] Galanopoulos, A., 1956, "The Seismic Risk At Athens, Praktika Akadimias Athenon," Proc. Acad. Athens), **31**, pp. 464–472. In Greek.
[27] Business Wire, Inc., 2019, Energy Vault Closes Series B Funding with $110 Million Investment from Softbank Vision Fund, https://www.businesswire.com/news/home/20190814005008/en/Energy-Vault-Closes-Series-B-Funding-With-110-Million-Investment-From-Softbank-Vision-Fund
[28] Andrade, J. E., Rosakis, A. J., Conte, J. P., Restrepo, J. I., Gabuchian, V., Harmon, J. M., Rodriguez, A., Nema, A., and Pedretti, A. R., 2021, "Seismic Performance Assessment of Multiblock Tower Structures As Gravity Energy Storage Systems," ASME J. Appl. Mech., Submitted.
[29] Gabuchian, V., Rosakis, A. J., Andrade, J. E., Harmon, J. M., Restrepo, J. I., Conte, J. P., Rodriguez, A., Nema, A., and Pedretti, A. R., 2021, "Multiscale Experiments for Seismic Performance Assessment of Multiblock Tower Structures for Energy Storage: 1/107 Scale," Earthq. Eng. Struct. Dyn.
[30] Restrepo, J. I., Conte, J. P., Rodriguez, A., Gabuchian, V., Nema, A., Andrade, J. E., Rosakis, A. J., and Pedretti, A. R., 2021, "Multiscale Experiments for Seismic Performance Assessment of Multiblock Tower Structures for Energy Storage: 1/25 Scale," Earthq. Eng. Struct. Dyn.
[31] Harmon, J. M., Andrade, J. E., Rosakis, A. J., Gabuchian, V., Restrepo, J. I., Conte, J. P., Rodriguez, A., Nema, A., and Pedretti, A. R., 2021, "Using the Level Set Discrete Element Method for Predicting the Seismic Performance of Frictional Structures at Multiple Scales," Comput. Method Appl. M., **20**.
[32] Kawamoto, R., Andò, E., Viggiani, G., and Andrade, J. E., 2016, "Level Set Discrete Element Method for Three-Dimensional Computations with Triaxial Case Study," J. Mech. Phys. Solids, **91**, pp. 1–13.
[33] Sutton, M., Orteu, J., and Schreier, H., 2009, *Image Correlation for Shape, Motion, and Deformation Measurements*, 1st ed., Springer US.